New ages, morphometric and geochemical data on recent shoshonitic volcanism of the Puna, Central Volcanic Zone of Andes: San Jerónimo and Negro de Chorrillos volcanoes

Jose-Luis Fernandez-Turiel, Julio Saavedra, F. J. Perez-Torrado, A. Rodriguez-Gonzalez, Marta Rejas, Hervè Guillou, Meritxell Aulinas

Journal of South American Earth Sciences 109 (2021) 103270

Contents lists available at ScienceDirect

Journal of South American Earth Sciences

journal homepage: www.elsevier.com/locate/jsames

New ages, morphometric and geochemical data on recent shoshonitic volcanism of the Puna, Central Volcanic Zone of Andes: San Jerónimo and Negro de Chorrillos volcanoes

J.L. Fernandez-Turiel [a,*], J. Saavedra [b], F.J. Perez-Torrado [c], A. Rodriguez-Gonzalez [c], M. Rejas [a], H. Guillou [d], M. Aulinas [e]

[a] Geosciences Barcelona, GEO3BCN, CSIC, Barcelona, Spain
[b] IRNASA, CSIC, Salamanca, Spain
[c] Instituto de Estudios Ambientales y Recursos Naturales (i–UNAT), Universidad de Las Palmas de Gran Canaria (ULPGC), Las Palmas de Gran Canaria, Spain
[d] Laboratoire des Sciences Du Climat et L'Environnement, CEA-CNRS-UVSQ, Gif-sur-Yvette, France
[e] Departament de Mineralogia, Petrologia I Geologia Aplicada Facultat de Ciències de La Terra, Universiat de Barcelona, Spain

ARTICLE INFO

Keywords:
Shoshonite
Phlogopite
Dusty plagioclase
Glass
Central Volcanic Zone
Andes

ABSTRACT

Shoshonitic volcanic centres are scarce within the back-arc mafic volcanism of the Puna Plateau in the Central Volcanic Zone of the Andes. San Jerónimo and Negro de Chorrillos volcanoes are two well preserved shoshonitic monogenetic edifices that developed mainly Strombolian activity and lava flows, which extended more than 9 and 4 km from the vent, producing a volume DRE (Dense Rock Equivalent) of 0.091 and 0.020 km^3, respectively. The new unspiked K–Ar (groundmass) ages of San Jerónimo (144 ± 3 ka) and Negro de Chorrillos (51 ± 2 ka) eruptions presented in this work are both younger than those previously published. Petrographic and compositional features allow distinguishing between potassic and ultrapotassic suites in volcanic products of both eruptions. Phlogopite occurrence and low glass content characterize the ultrapotassic suite. Based on the crustal thickness of this part of the Puna and the experimental constraint, these magmas last equilibrated at Moho depths at around 50 km (the highest depth of spinel lherzolite stability field) for temperatures of 1100–1200 °C. Once in the crust, the K-rich magma underwent a minor interaction with a trachytic-trachydacitic melt, which is evidenced petrographically and geochemically, e.g., mismatch of mineral assemblages (co-occurrence of olivine and quartz), disequilibrium crystal textures (dusty zones in plagioclase, embayments in sanidine), and a wide range of compositional variation in the glasses. Ultrapotassic (i.e., phlogopite-bearing) and potassic lavas in the same eruption are interpreted as pulses of the same magma but with a longer mixing time with the trachytic-trachydacitic melt for the resulting ultrapotassic rocks within an eruptive time frame of hours or days. The singular shoshonitic character of these magmas could be related to their origin along an old terrane boundary. Afterwards, as occurs for other mafic magmas of the Puna, major NW-SE fault systems would favour their ascent to the surface.

1. Introduction

The Central Volcanic Zone of the Andes (CVZ; e.g., Thorpe, 1984; Stern, 2004) extends between 14° S in Peru and 27° S in Chile and Argentina (Fig. 1) and records a complex evolution of a volcanic arc and back-arc through hundreds of volcanoes, from constructional (polygenetic and monogenetic) to large collapse calderas (Grosse et al., 2017; Guzmán et al., 2014; Kay and Coira, 2009; Maro et al., 2016b, 2017; Naranjo et al., 2018; Petrinovic et al., 2017; Tilling, 2009). The preservation of volcanic edifices is usually exceptional due to the prevailing arid or hyperarid conditions since early to middle Miocene times (Stern et al., 2007; Strecker et al., 2007). The CVZ overlaps the Central Andean Plateau or Altiplano-Puna Plateau, a ~4–7 km elevation region with the thickest continental crust on Earth, reaching up to 80 km in some areas (Allmendinger et al., 1997; Beck et al., 2015; Liu et al., 2011; Naranjo et al., 2018; Wörner et al., 2018; Yuan et al., 2002). It is the most

* Corresponding author.
E-mail addresses: jlfernandez@geo3bcn.csic.es (J.L. Fernandez-Turiel), franciscojose.perez@ulpgc.es (F.J. Perez-Torrado), alejandro.rodriguezgonzalez@ulpgc.es (A. Rodriguez-Gonzalez), mrejas@geo3bcn.csic.es (M. Rejas), herve.guillou@lsce.ipsl.fr (H. Guillou), meritxellaulinas@ub.edu (M. Aulinas).

https://doi.org/10.1016/j.jsames.2021.103270
Received 23 September 2020; Received in revised form 2 March 2021; Accepted 2 March 2021
Available online 10 March 2021

extensive orogenic plateau on Earth formed in an oceanic-continental subduction setting (Garzione et al., 2017). This plateau consists of two morphotectonic units, the Altiplano (~14–23° S) and Puna (~23–27° S). In this geotectonic setting, the magmatism is driven by the geodynamic mechanisms of plateau uplift and the processes by which the continental crust overriding plate has been shortened and thickened, whereas the mantle lithosphere that originally underlay it has been thinned or entirely removed (Beck et al., 2015; Garzione et al., 2017; Kay and Coira, 2009). These processes produced variations in the crustal thickness of the plateau. This thickness is around 50 km depth in the studied area (~24–25° S) (Beck et al., 2015; McGlashan et al., 2008; Yuan et al., 2002).

The Andean CVZ's volcanic activity is located in both the frontal arc and the back-arc from Miocene to Quaternary (e.g., Barnes and Ehlers, 2009; Jiménez and López-Velásquez, 2008; Kay and Coira, 2009; Mamani et al., 2010). Polygenetic volcanism produced stratovolcanoes with associated andesitic to dacitic pyroclastic fall deposits and lava flows, and dacitic to rhyolitic domes and pyroclastic flow deposits, mainly in the frontal volcanic arc, although there are also some scarce stratovolcanoes in the back-arc, e.g., Tunupa (Salisbury et al., 2015), Uturuncu (Michelfelder et al., 2013; Sparks et al., 2008), and Tuzgle (Coira and Kay, 1993; Norini et al., 2014). Caldera-sourced silicic deposits occur throughout the Altiplano-Puna plateau, being less abundant and generally younger in the south than in the north (Guzmán et al., 2014; Kay et al., 2010; Schnurr et al., 2007). For example, the Cerro Blanco Volcanic Complex produced 4.2 ka BP ago, one of the most important Holocene eruptions in the world (Fernandez-Turiel et al., 2019). In the back-arc, monogenetic eruptive centres generated andesitic to basaltic andesitic, and minor shoshonitic, pyroclastic fall deposits and lava flows (Acocella, 2014; Báez et al., 2017; Grosse et al, 2017, 2020; Haag et al., 2019; Naranjo et al., 2018; Wörner, 2019) as well as some pyroclastic felsic deposits (Filipovich et al., 2020; Petrinovic et al., 2005; Petrinovic and Colombo Piñol, 2006).

Magmas of both constructional volcanoes and calderas ascend through and interact with the thick continental crust, mainly associated with N–S, NW-SE and NE-SW regional left-lateral strike-slip fault zones. For example, Lípez-Coranzulí, Calama-Olacapato-El Toro, Archibarca-Galán, and Culampajá-Farallón Negro fault zones (Acocella et al., 2011; Bonali et al., 2012; Lanza et al., 2013; Naranjo et al., 2018; Norini et al., 2013; Petrinovic et al., 2017; Tibaldi et al., 2017; Tibaldi and Bonali, 2018).

The mafic back-arc volcanic centres in the Puna plateau are isolated, loosely clustered or form small volcanic fields (Báez et al., 2017; Garzione et al., 2017; Maro et al., 2016b). The eruptions, mainly of Strombolian style, produced basaltic andesites to andesites with a high-K calc-alkaline signature, and less frequently basaltic trachyandesites and trachyandesites that are at or near shoshonite composition (Déruelle, 1991; Drew et al., 2009; Guzmán et al., 2006; Kay et al., 1994; Knox et al., 1989; Krallmann, 1994; Maro et al., 2017; Murray et al., 2015; Richards et al., 2006; Risse et al., 2013, 2008). Shoshonitic monogenetic volcanoes are distributed in the central Andean back-arc region of Peru (Carlier et al., 2005; Sandeman and Clark, 2004), Bolivia (Hoke and Lamb, 2007; Jiménez and López-Velásquez, 2008; Redwood and Rice, 1997; Salisbury et al., 2015), and Argentina (Déruelle, 1991; Guzmán et al., 2006; Kay et al., 1994; Krallmann, 1994; Schreiber and Schwab, 1991).

The direct partial melting of the primitive mantle cannot produce shoshonitic magmas, so an additional source of K_2O is needed. This enrichment of K_2O and K/Na within the mantle is currently explained by (Förster et al., 2019): 1) a two-stage fusion model of the "vein + wall rock" metasome (Foley, 1992), and 2) a single-stage recycled sediment/crust model (Campbell et al., 2014). The first model is the most suitable for the Andean potassic magmas (e.g., Carlier et al., 2005; Hoke and Lamb, 2007; Murray et al., 2015). In this framework, the potassic and ultrapotassic magmas are the earliest melts to be generated when the metasomatized lithospheric mantle undergoes heating and/or extension (Gibson et al., 1995). The study of shoshonitic volcanoes can provide insights regarding the mantle composition and mantle-crust

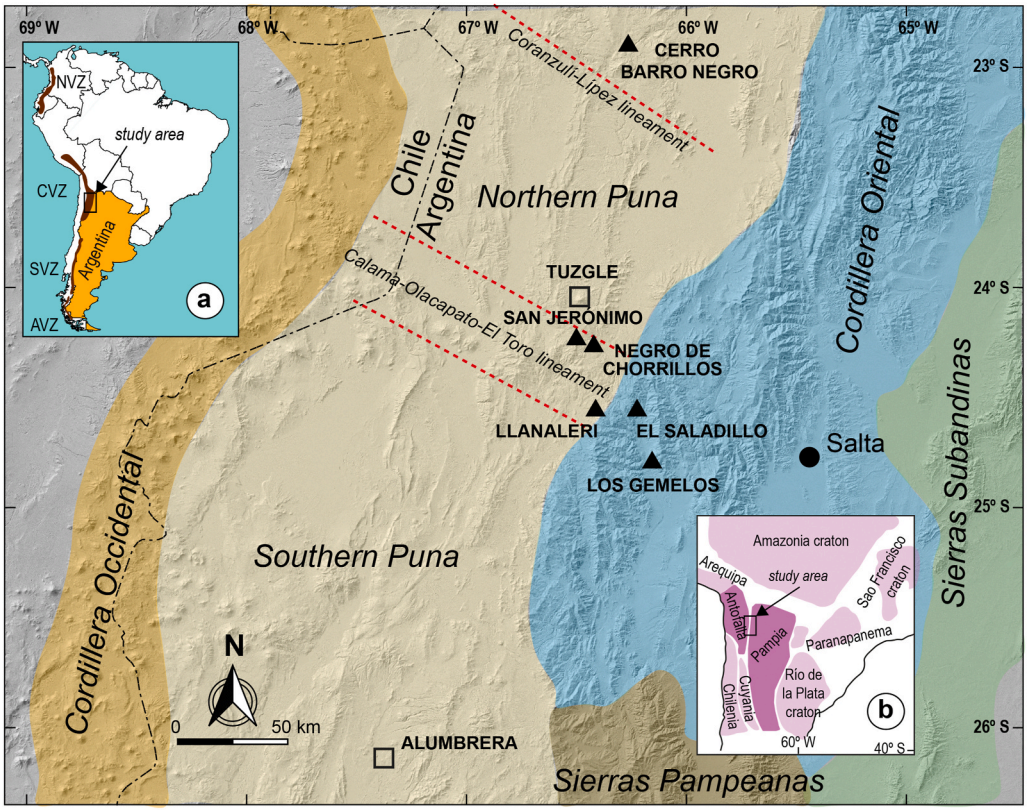

Fig. 1. Location of studied San Jerónimo and Negro de Chorrillos and other shoshonitic volcanic centres in the Puna Plateau (triangles). The squares indicate other volcanoes mentioned in the text. The shaded-relief image is derived from ASTER GDEM ver.3 (https://ssl.jspacesystems.or.jp/ersdac/GDEM/E/). Inset (a) shows the location in the Andes of the Northern Volcanic Zone (NVZ), the Central Volcanic Zone (CVZ), the Southern Volcanic Zone (SVZ), and the Austral Volcanic Zone (AVZ). Inset (b) displays the cratons and Palaeozoic terranes in southern South America (modified from Franceschinis et al., 2016).

interaction of discrete lithospheric mantle domains at continental subduction zones (Carlier et al., 2005; Jiménez and López-Velásquez, 2008). On the other hand, the use of xenoliths as proxies of the mantle composition is limited by their scarcity in this type of mafic volcanism (e.g., Chapman et al., 2015; Maro et al., 2016a; McLeod et al., 2013), which limits its use to know the mantle composition.

San Jerónimo (SJ), also called in the literature San Gerónimo, and Cerro Negro de Chorrillos (NdC), sometimes called Cerro Chorrillos, are two of the most representative back-arc monogenetic shoshonitic volcanoes in the Puna plateau (Déruelle, 1982, 1991; Ducea et al., 2013; Harmon et al., 1984; Hörmann et al., 1973; Kay et al, 1994, 1999; Knox et al., 1989; Krallmann, 1994; Murray et al., 2015; Petrinovic, 2008; Schreiber and Schwab, 1991; Tannhäuser, 1906; Urquizo Furlán, 2012) (Fig. 2). Although the studies mentioned above contributed to advancing knowledge of the particular history and petrogenesis of these monogenetic shoshonitic volcanoes, their origin and age have remained controversial. SJ and NdC volcanoes are particularly well suited for a petrological study as they have erupted shoshonitic lavas with a wide variety of mineral contents and textures. Earlier studies have provided representative volcanological (Urquizo Furlán, 2012), petrographic and whole-rock and mineral chemistry data of SJ and NdC (Déruelle, 1982, 1991; Ducea et al., 2013; Harmon et al., 1984; Hörmann et al., 1973; Kay

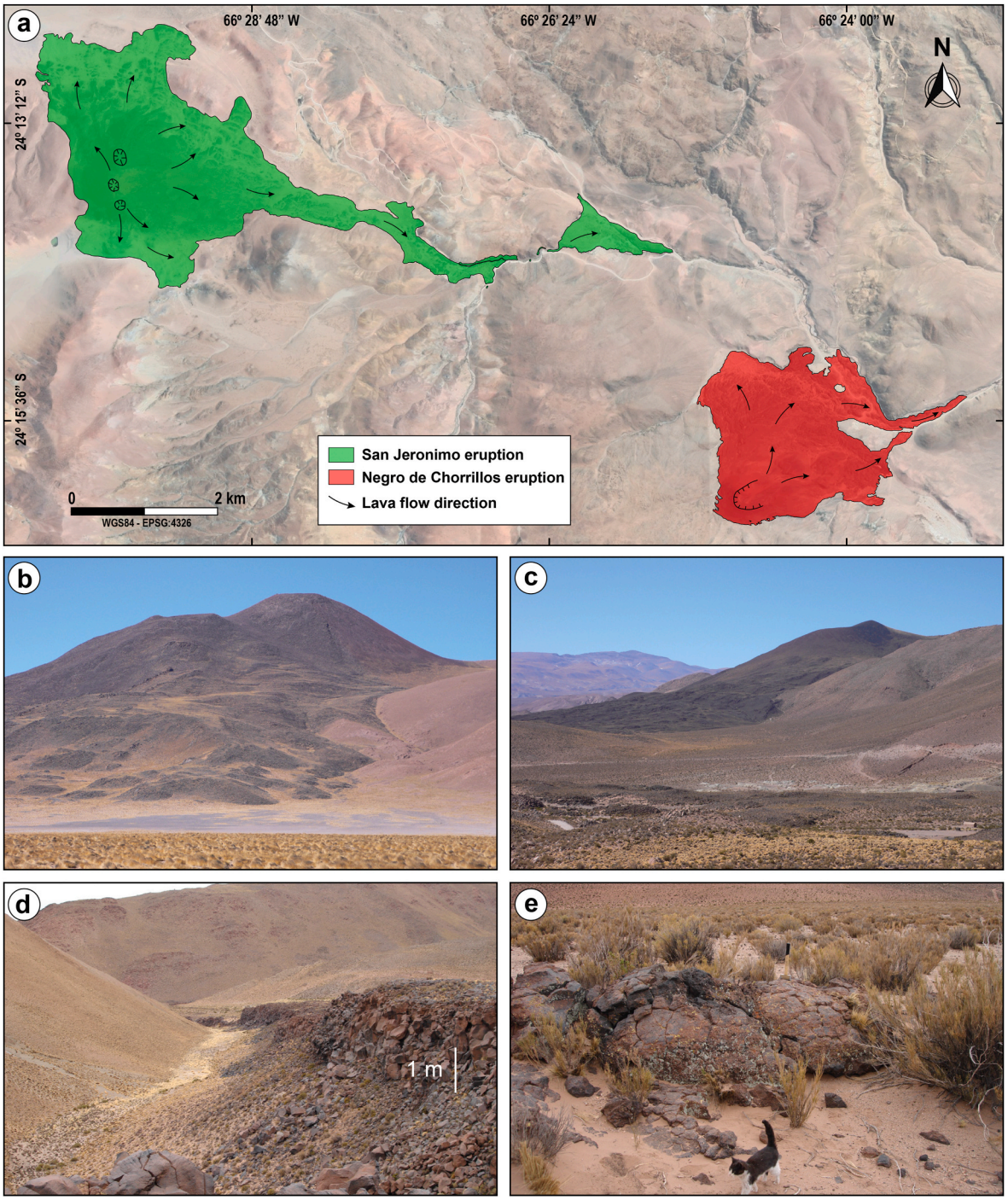

Fig. 2. a) Satellite image (from Google Earth, August 3, 2016, CNES/AIRBUS) of study area showing the location of San Jerónimo and Negro de Chorrillos volcanic centres. b-e) Field photographs of San Jerónimo volcano from NW (b); Negro de Chorrillos volcano from NW (c); blocky lava flow of San Jerónimo (d); and blocky lava flow of Negro de Chorrillos (e).

et al, 1994, 1999; Knox et al., 1989; Krallmann, 1994; Murray et al., 2015; Schreiber and Schwab, 1991; Tannhäuser, 1906). In this sense, we expand on these studies and aim to provide a more comprehensive overview of the volcanic history of SJ and NdC. We present new geomorphological, petrological, geochemical and dating constraints to further understand their magmatic plumbing system and the evolution of shoshonitic magmas in the Altiplano-Puna Plateau as in other geodynamic settings.

2. Geological setting

The study area is on the Calama-Olacapato-El Toro (COT) fault zone at the transition or limit between the northern and southern Puna (Fig. 1). The COT fault zone transversally crosses, from NW to SE, the volcanic arc and back-arc regions of the Puna plateau, at about 22–25°S. The COT is a NW–SE trending left-lateral transcurrent fault zone with inferred transtensive motions that, in the study area and during the late Pliocene–Quaternary, responds to a kinematic regime of a left-lateral strike-slip with a horizontal ~ E–W σ_1 and ~N–S σ_3 (Lanza et al., 2013). The overall left-lateral transtension of this fault zone created favourable tectonic conditions for the ascent of magma and the associated volcanic activity in the back-arc, developing volcanic centres such as San Jerónimo and Negro de Chorrillos (Fig. 1) (Acocella, 2014; Bonali et al., 2012; Norini et al., 2013; Petrinovic et al., 2017; Riller et al., 2001), which in turn are affected by numerous WNW- to NW-striking subvertical fault scarps and associated aligned ponds and springs (Bonali et al., 2012; Lanza et al., 2013; Seggiaro et al., 2016). The magmatic activity along the COT lineament suggests that these lithospheric weakness zones control mantle melting by focusing thermal inputs and fluid ingress in the Puna lithospheric blocks, as was inferred for potassic and ultrapotassic melts in the large lineaments of the Altiplano (Carlier et al., 2005).

The volcanoes of San Jerónimo and Negro de Chorrillos are located 18 and 10 km west of the town of San Antonio de Los Cobres, respectively. The basement of San Jerónimo is formed by Miocene ignimbrites and the one of Negro de Chorrillos by Ordovician sediments, volcanic rocks and granitoids (Seggiaro et al., 2016). The edifice of San Jerónimo (24.2290°S 66.4985°W) consists of a monogenetic scoria cone, which closed a ravine in the south, forming an ephemeral lake (Vilela, 1969), and lava flows reaching 2–3 km to the north and ~9 km to the east from the vent. Negro de Chorrillos is also a monogenetic volcano (24.2715°S 66.4148°W), which in addition to a scoria cone, forms 2–5 km long lava flows to the north and east (Vilela, 1969), generated in three phases with effusive and explosive events (Urquizo Furlán, 2012). The second phase products are distinguished by the presence of phlogopite (Urquizo Furlán, 2012). Some authors have associated pyroclastic flows and ash fallout with this eruption (Seggiaro et al., 2016).

3. Methods

A palaeogeomorphological reconstruction of San Jerónimo and Negro de Chorrillos eruptions, based on fieldwork, was carried out to obtain the pre- and post-eruption terrain models following the methods developed by Rodriguez-Gonzalez et al. (2011, 2012). Field studies consisted of examining and identifying the different volcanic units (volcanic cone, lava flows and pyroclastic fall deposits) and the kind of relief below the volcanic deposits. The resulting information was implemented in a Geographical Information System (GIS), together with high-resolution optical images and present-day Digital Elevation Model (DEM) from Google Earth™, to proceed with the morphometric analysis. The GIS software used was TNTgis 2019 (MicroImages, Inc.). The generation of the DEM consisted of three general steps. The elevation point data of two areas containing the SJ and NdC volcanoes in Google Earth™ were extracted In the first step. The elevation point data extraction was performed with an online tool (Terrain Zonum Solution, http://www.zonums.com/gmaps/terrain.php). The coordinates (latitude and longitude in WGS84 projection) and the elevation (z) in meters for each elevation point sampled were the extraction process's output. These values were then imported into a text file for further process. Once revised for outliers, the second step comprised the generation of a contour map (5 m interval). Finally, the third step consisted of constructing a DEM from the contour lines. A 5 m DEM resolution was appropriate for the accurate quantification of all the morphometric parameters of interest. The second step's contour map (i.e., post-eruption) was also used to generate the pre-eruptive DEM, modifying the contour lines to obtain the pre-eruptive surface based on fieldwork (Rodriguez-Gonzalez et al., 2010). The comparison of pre- and post-eruption surfaces allowed us to

Table 1
Morphometric parameters of San Jerónimo and Negro de Chorrillos volcanoes.

Volcanic cone	Units	San Jerónimo			Negro de Chorrillos
Crater		North	Central	South	
Crater rim maximum elevation	M	4885	4950	4915	4425
Crater rim major axis (acr)	M	164	152	157	448
Crater rim minor axis (bcr)	M	144	83	117	350
Crater rim eccentricity (ecr)		0.5	0.7	0.8	0.6
Crater major axis azimuth (theta)	Degrees	170	163	143	70
Crater depth (hcr)	M	3	3	4	75
Cone major axis (aco)	M		1846		1188
Cone minor axis (bco)	M		1340		1047
Cone eccentricity (eco)			0.7		0.5
Cone major axis azimuth (theta)	degrees		366		30
Cone height (h)	M		258		162
Cone volume (V)	km^3		0.118		0.034
Cone volume DRE (V_{DRE})	km^3		0.030		0.009
Area (A)	km^2		1.904		0.699
Cone slope (beta)					
Median	degrees		20		20
Mean	degrees		21		19
Minimum	degrees		0		0
Maximum	degrees		45		45
Standard deviation	degrees		8		8
Basement slope (pre-eruption)					
Median	degrees		8		16
Mean	degrees		9		15
Minimum	degrees		0		0
Maximum	degrees		39		40
Standard deviation	degrees		6		6
Lava flow					
Length (L)	m		9390		4520
Bottom width (wb)					
Median	m		444		767
Mean	m		913		1034
Minimum	m		26		61
Maximum	m		3287		2437
Standard deviation	m		960		868
Area (A)	km^2		8.801		4.631
Height (h) (thickness)					
No. Profiles for calculation			93		45
Median	m		11		8
Mean	m		12		11
Minimum	m		3		2
Maximum	m		22		33
Standard deviation	m		5		8
Volume (V)	km^3		0.081		0.015
Volume DRE (V_{DRE})	km^3		0.061		0.011
Lava flow basis slope					
Median	degrees		8		8
Mean	degrees		11		8
Minimum	degrees		0		0
Maximum	degrees		31		20
Standard deviation	degrees		7		6

estimate cone and lava flow volumes and morphometric parameters (Table 1). Surface modification by the pyroclastic sheet-like fall deposits was almost imperceptible because of their low magnitude, and hence their volumes were not estimated. These cone and lava flow bulk volume estimates were transformed into Dense Rock Equivalent (DRE) volumes considering a porous volume fraction of 75% for pyroclasts in the cones (Mangan and Cashman, 1996) and 25% for basaltic a'a' lava flows (Wolfe, 1988).

Three representative sites from the SJ lava flows and other three from the NdC lava flows were sampled based on the suitability for K–Ar dating as well as for petrological and geochemical studies (Fig. 3). The identification number IGSN of samples was registered by SESAR: SJ-1 has IGSN IEJLF001T, SJ-2 is IEJLF001U, SJ-5 is IEJLF001V, NdC-3 is IEJLF001W, NdC-6 is IEJLF001X, and NdC-7 is IEJLF001Y. We also sampled the Alumbrera volcano (Fig. 1), near the town of Antofagasta de la Sierra, a recent mafic eruption of the Puna only for dating to compare the ages, i. e., CB3001-D registered with IGSN IEJLF001Z.

Petrography and modal mineralogy were performed by conventional optical petrographic microscopy. For modal analysis, 1000 points per sample were counted. All whole-rock samples were crushed and

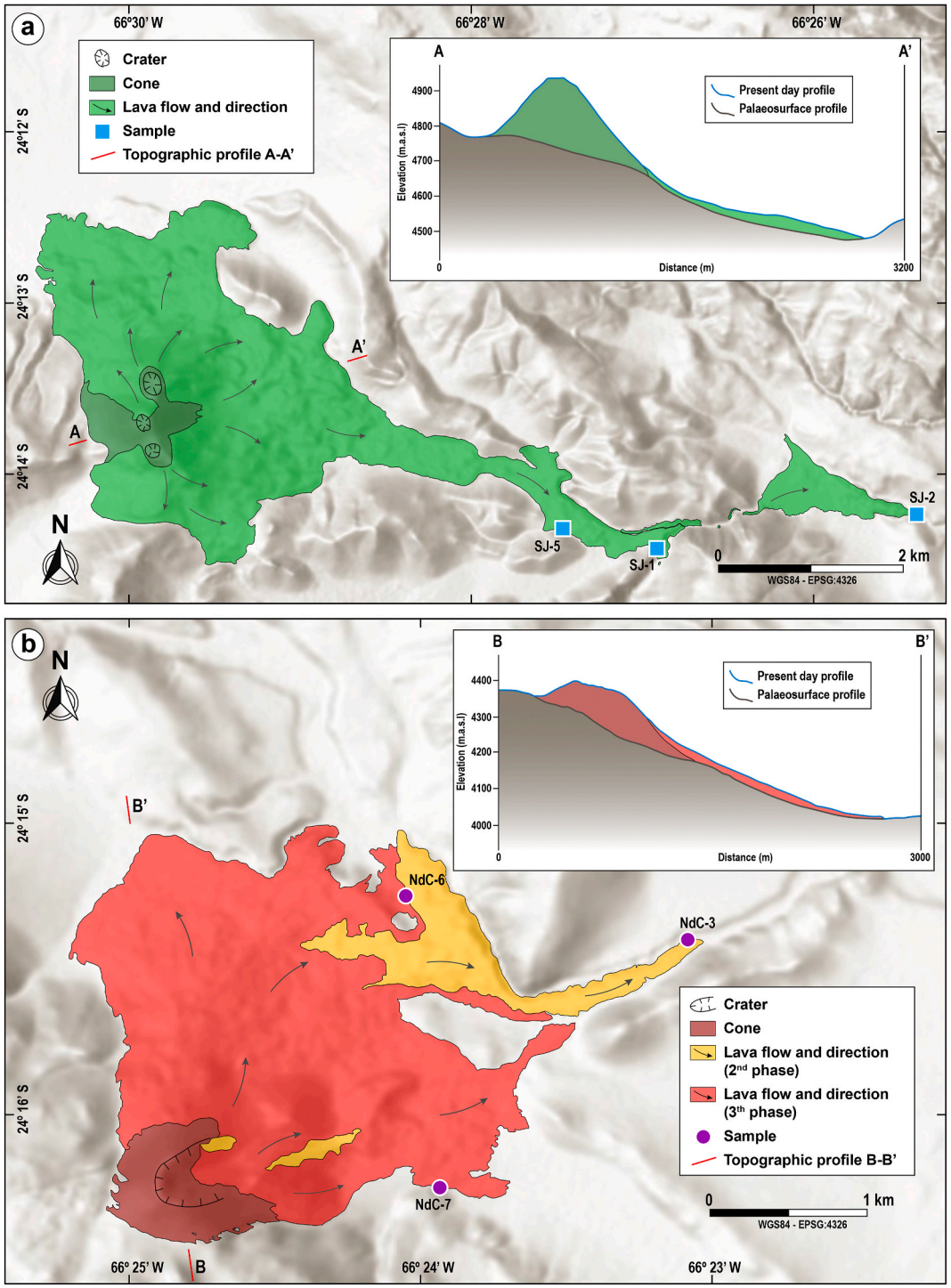

Fig. 3. Deposits and structures of San Jerónimo (a) and Negro de Chorrillos (b) volcanoes. The eruptive phases are according to Urquizo Furlán (2012). The insets show topographic profiles of the palaeosurface before the eruption and the present-day topography.

powdered using standard jaw crusher and agate milling equipment. Major and some trace elements (Ba, Cr, Ni, Rb, Sr, V, Y, Zn and Zr) were determined by X-ray fluorescence (XRF) spectrometry at the Scientific and Technological Centres of the University of Barcelona (CCiTUB), using a Philips PW2400 sequential X-Ray spectrometer with a Rh tube, by fusion of 2 g of powdered sample with lithium tetraborate to make glass beads and then analysed by XRF for major elements. Pressed powder pellets with 5 g of sample were used for trace element XRF analysis. Additional trace elements (Nb, Ta, Cs, Hf, Pb, Th, U and the rare Earth elements or REE) were analysed by High Resolution-Inductively Coupled Plasma-Mass Spectrometry (HR-ICP- MS, Element XR, Thermo Scientific) at the Laboratory of Geochemistry labGEOTOP (GEO3BCN, CSIC, Barcelona). A split of 0.1 g of each sample was digested with HNO_3:$HClO_4$:HF (2.5:2.5:5 ml, v/v), doubly evaporated to incipient dryness with the addition of HNO_3, and finally made up to 100 ml with 1% (v/v) HNO_3; before to HR-ICP-MS measures, a known amount of indium was added as the monitor. The precision and accuracy of analytical determinations were monitored using reference materials of the Geological Survey of Japan (rhyolite JR-3 and basalt JB-3).

The compositions of olivine, pyroxenes, phlogopite, feldspars, spinel and other minor minerals as well as of glasses were analysed in situ at the CCiTUB using an electron microprobe analyser (EMPA) Cameca SX50. An acceleration voltage of 20 kV and a current beam of 15–20 nA were used during all the analyses except for sodium. A current beam of 6 nA and an incident electron beam of 5–10 μm diameter were used to minimise the sodium loss. The instrument was calibrated using primary natural and synthetic standards. The quality of mineral analyses was reviewed, verifying that the structural formula gave a correct stoichiometry.

Treatment of whole-rock and mineral chemistry data was performed with GCDkit version 6.0 (Janoušek et al., 2006, 2016). Mg number, Mg# = (100 x Mg/[Mg + Fe^{2+}]), was calculated assuming 10% of the iron present in the melt as Fe^{3+} and the remaining 90% as Fe^{2+} (Gill, 2010). Europium anomalies (Eu/Eu*) were calculated as $Eu/Eu^* = (Eu)_{cn}/[(Sm)_{cn} \times (Gd)_{cn}]^{0.5}$; cn, normalized to chondrite from Boynton (1984). Values of εNd were used with published Nd isotope ratios and $(^{143}Nd/^{144}Nd)_{CHUR} = 0.512638$.

Whole-rock major and trace element concentrations of this study (Fernandez-Turiel et al., 2020) were compiled in a larger dataset together with previously reported geochemical data for SJ and NdC lava flows (Déruelle, 1991; Hörmann et al., 1973; Kay et al., 1994; Krallmann, 1994; Murray et al., 2015; Schreiber and Schwab, 1991), and with other Puna shoshonitic centres: Los Gemelos and El Saladillo (Guzmán et al., 2006; Hausen, 1937; Hörmann et al., 1973; Kay et al., 1994; Krallmann, 1994), Llanaleri (Krallmann, 1994) and Cerro Barro Negro (Maro et al., 2016b) (Fig. 1). This shoshonitic dataset consists of 54 samples. As reference, the whole-rock major and trace element concentrations and Pb, Sr, Nd isotope data of the Neogene mafic volcanic rocks of northern Puna (Kay et al., 2010; Krallmann, 1994; Maro et al., 2016b) and southern Puna (Báez et al., 2017; Drew et al., 2009; Risse et al., 2013) were also compiled.

Magnetostratigraphy was used in combination with isotopic dating and geomorphological observations to provide the most reliable time framework for volcanic deposits' geological reconstruction. The preliminary definition of polarity sequences was carried out in the field using a portable fluxgate magnetometer. After these paleomagnetic works, two samples of lava flows were selected for age determinations: SJ-2 from San Jerónimo volcano and NdC-3 from Negro de Chorrillos volcano. Samples were K–Ar dated at the Laboratoire des Sciences du Climat et de l'Environnement (LSCE) at Gif-sur-Yvette (France), using the unspiked K–Ar method (Charbit et al., 1998). Groundmass splits from fresh samples were prepared (Guillou et al., 1996), and age calculations were based on the decay and abundance constants from Steiger and Jäger (1977). The samples were crushed and sieved to 0.250–0.125 mm size fraction and ultrasonically washed in HNO_3 to remove phases formed by alteration. Both K and Ar measurements were performed on the groundmass, which is considered representative of the phase that crystallized during the lavas' solidification. Phenocrysts and xenocrysts, which may carry excess ^{40}Ar, were removed using heavy liquids of appropriate densities, magnetic separations and final inspection under binocular picking microscope. Potassium was analysed by ICP-MS. Argon was extracted from 1 to 2.5 g groundmass samples by radio-frequency heating induction in a high vacuum glass line and purified with titanium sponge and Zr–Al getters. Argon was analysed using a 180°, 6 cm radius, 620 V accelerating potential mass spectrometer working in a semi-static mode. The isotopic composition of Ar and Ar content were determined using an unspiked K–Ar technique (Charbit et al., 1998; Guillou et al., 1996).

4. Results

4.1. Morphometry

Table 1 shows the values of the most significant morphometric parameters, including areas and volumes, of cones and lava flows of SJ and NdC. SJ has a multiple cone with three closed craters roughly aligned NNW-SSE (Figs. 2–3), reaching a maximum altitude of 4950 m a.s.l. At the central crater. It covers a surface of about 1.9 km^2 and is 258 m high. The median slope of the cone flanks is 20, with a maximum of 45°. It developed on a palaeotopography where the median slope was 9°, although reaching 39° in some places (Fig. 3a). NdC has a horseshoe-shaped cone with a crater open towards the NE in the main direction of the basement's prevalent slope (Figs. 2–3). The maximum altitude is 4425 m a.s.l. The surface of this cone is 0.7 km^2, and it is 162 m high. The median of the NdC cone is also 20, with a maximum of 45° (Fig. 3b).

The lava flows of SJ and NdC consist of blocky-type lava and, exceptionally, a'a'-type lava with typical scoriaceous and very fragmented surface (Fig. 2d–e). The lava flows of SJ cover an area of 8.8 km^2 and those of NdC 4.6 km^2. The maximum lengths reached by these flows were 9.4 and 4.5 km from SJ and NdC vents, respectively. The thickness of the lava flows varies between 1 and 5 m, although sometimes several lava lobes overlap, reaching up to 20 and 30 m thickness in SJ and NdC, respectively.

Pyroclastic sheet-like fall deposits have not been considered in volume estimates due to their small occurrence. According to the methodology, the comparison between the generated pre- and post-eruption DEMs allow estimating the cone and lava flow bulk volumes, as represented schematically in Fig. 3 (insets). In this way, the bulk volumes estimated for cone and lava flows of SJ are 0.118 and 0.081 km^3, respectively (Table 1). The corresponding Dense Rock Equivalent (DRE) volumes for SJ are 0.030 and 0.061 km^3. For the NdC volcano, the bulk volume estimates are 0.034 and 0.015 km^3 for cone and lava flows, and 0.009 and 0.011 km^3 expressed as DRE volumes. Thus, the total volume DRE (Dense Rock Equivalent) was 0.091 and 0.020 km^3 for SJ and NdC volcanoes, respectively. It is noted that the lava flow DRE volumes are greater than the cone DRE volumes in both cases, being the lava-to-cone ratio of 2.0 in SJ and 1.2 in NdC.

4.2. Petrography

Both SJ and NdC lavas have a general hipocrystalline, porphyritic-aphanitic, vesicular texture with macrocrysts (0.2 and up to 7 mm) of olivine, clino- and orthopyroxene, quartz, feldspars and, in some cases, phlogopite in a very fine-grained, commonly glassy, groundmass with microcrysts (<0.2 mm) of feldspars (plagioclase and sanidine), clinopyroxene, olivine, opaque minerals and apatite. Xenoliths were not observed in the field.

The occurrence of phlogopite allows separating the samples into two groups. We have observed this mineral in samples of the second phase of NdC eruption (NdC-3 and NdC-6) but not in the sample of the third phase (NdC-7). Phlogopite was not observed in SJ's longest lava flow (samples SJ-1, SJ-2, SJ-5; Table 2). Samples without phlogopite present

Table 2
Petrography: modal analysis (% in volume).

Sample	Potassic series				Ultrapotassic series	
	SJ-1	SJ-2	SJ-5	NdC-7	NdC-3	NdC-6
Phenocrysts						
Olivine	5.9	6.4	10.7	6.8	8.5	7.8
Pyroxene	4.2	2.9	2.4	3.4	0.9	2.0
Cpx (corona)	0.6	1.1	1.4	0.4	0.4	1.6
Phlogopite	–	–	–	–	6.9	3.8
Apatite	tr	tr	tr	tr	0.1	0.1
Xenocrysts						
Quartz	1.4	1.2	2.3	0.8	0.5	2.2
Feldspar	0.1	0.1	0.7	0.1	0.6	0.9
Matrix						
Feldspar	23.1	42.1	25.6	42.9	37.5	35.2
Apatite	1.1	1.3	1.0	2.0	3.1	2.3
Cpx	4.7	10.9	13.3	12.7	25.8	17.5
Opaque minerals	7.2	6.6	5.8	11.7	14.5	8.1
Glass	37.1	14.2	32.1	14.7	0.4	2.1
Vesicles	14.6	13.2	4.7	4.5	0.8	16.4
Total	100	100	100	100	100	100

porphyric (11–17 vol % macrocrysts, ranging ~200 μm to 5 mm in size), vesicular (4–15 vol % vesicles), and sometimes glomeroporphyric textures with pyroxenes enclosing spinel inclusions (Fig. 4a). They have a glassy to fine-grained, plagioclase-dominated microlite groundmass, showing a fluidal texture (more evidenced in SJ-2 and NdC-7), with macrocrysts of olivine (sometimes with reaction rims), feldspars, clinopyroxene and rare orthopyroxene. Plagioclase macrocrysts are often corroded and show a sieve texture defined by a core, a dusty or fritted zone, and a rim (Fig. 4b). The dusty texture consists of a diffuse zone that mantles the crystal's interior, as defined by Tsuchiyama (1985). It varies in thickness, entering into the pre-existing crystal from the margin inward and sometimes extending throughout its core. An overgrowth of clear plagioclase invariably mantles the dusty zone. Sanidine is very scarce and occurs as macrocrysts of ~200 μm to 3 mm in size. Euhedral to subhedral olivine macrocrysts and microcrysts often show corrosion gulfs (Fig. 4c). Subhedral-euhedral pyroxene macrocrysts show variable sizes (0.2–6 mm). Olivine and pyroxene macrocrysts include tiny opaque minerals.

Phlogopite-bearing lavas are texturally similar to the previous ones, although the macrocryst content is higher (≈18 vol %), being olivine and phlogopite the main mineral phases. Phlogopite mainly occurs as macrocrysts (3.8–6.9 vol %, Table 2), with evident opacitic rims due to disequilibrium processes (Fig. 4d), and minor microcrysts. Sanidine occurs as corroded macrocrysts of ~200 μm to 3 mm in size (Fig. 4e) but is also very common in the groundmass as well as clinopyroxenes. Glass is much scarcer than in the previous group (0.4–2.1 vs. 14.2–37.1 vol %). There are also remnants of much-altered minerals, in part perhaps amphiboles.

One of the most striking features of the SJ and NdC lavas is the presence in the same sample of olivine and quartz macrocrysts. These peculiar quartz crystals, always in small quantities (0.5–2.3 vol %) (Table 2), do not show evidence of notable deformations (such as mosaic or wavy extinctions, intense fractures, etc.), but reaction coronas are common (Fig. 4f). The coronas consist of acicular clinopyroxene and glass rimming the quartz crystals. Where corrosion is scarce and the corona undeveloped, angular, automorphic or subautomorphic forms are observed.

4.3. Whole-rock geochemistry

The SJ and NdC samples of this work range from 53.19 to 57.44 wt % SiO_2, 6.31–7.72 wt % MgO, 3.56–5.98 wt % K_2O, 2.49–3.02 wt % Na_2O, and 1.02–2.12 wt % TiO_2. The volatile contents determined in the whole-rocks are 0.09–0.90 wt % LOI, and magnesium number (Mg#) ranges between 67 and 70, except for sample SH-7 with a Mg# of 60. All these samples, on anhydrous basis, are classified as basaltic trachyandesite and trachyandesite in the total alkalis-silica (TAS) diagram (Le Bas et al., 1986) (Fig. 5a). While SJ samples are mainly in the subalkaline field, the NdC samples are mostly in the alkaline field (Fig. 5a) (Irvine and Baragar, 1971). In the SiO_2 vs. K_2O diagram, the samples plot in the shoshonite series field (Fig. 5b) (Peccerillo and Taylor, 1976). According to the K_2O and Na_2O contents, most of the samples are potassic ($1 \leq K_2O/Na_2O \leq 2$ wt %), except for some lavas belonging to NdC volcanic edifice (i.e., NdC-3 and NdC-6), which are ultrapotassic ($K_2O/Na_2O \geq 2$ wt %, $K_2O > 3$ wt %, and MgO > 3 wt %) (Fig. 5c) (Foley et al., 1987; Gill, 2010). The two samples that are ultrapotassic are the two phlogopite-bearing samples. From the perspective of geotectonics, the studied rocks in the Yb–Ce plot reflect a continental magmatic arc setting (Gill et al., 2004) (Fig. 5d).

In a primordial mantle normalized diagram, all samples display enrichment in large-ion lithophile elements (LILE, K, Rb, Sr, Cs, Ba and light REE) with pronounced negative anomalies in some high-field strength elements (HFSE, i.e., Nb, Ta and Ti) and a positive anomaly of Pb and Li (Fig. 6a). Patterns of potassic and ultrapotassic lavas are similar in the general shape, but the last exhibit, in addition to the enrichment of K, slightly higher contents of Rb, Ba, Zr, and Hf.

REE patterns are similar for all lavas, with a steep slope pattern for light REE (LREE) ($(La/Dy)_n$, 12–14) that becomes practically flat in the Ho–Lu segment ($(Ho/Lu)_n$, 1.0–1.1), whereas the Eu anomaly is slightly marked (Eu/Eu*, 0.81 to 0.97) (Fig. 6b). In detail, ultrapotassic lavas of the NdC are slightly more enriched in all REE and, in the potassic lavas, sample NdC-7 overlaps considerably with the SJ lavas for La–Dy segment and with the NdC ultrapotassic lavas from Ho to Lu.

Harker diagrams show good negative correlations of Fe_2O_{3t} (Fig. 7a), MgO and CaO (Fig. 7b) with SiO_2. However, Al_2O_3, Na_2O, K_2O, TiO_2 and P_2O_5 plot poorly defined trends (not shown). Trace elements do not present simple trends (e.g., SiO_2 against Rb and Ba, Fig. 7c–d).

4.4. Mineral and glass compositions

Mineral and glass compositions are reported in an open dataset (Fernandez-Turiel et al., 2020). This section exposes the results obtained for olivine, pyroxene, phlogopite, feldspars, glass, and opaque minerals.

4.4.1. Olivine

The olivine composition from SJ and NdC lava flows ranges from Fo_{89} to Fo_{71} (mol % forsterite component) (Fig. 8a–c). Two separate groups can be distinguished. The most forsteritic olivine ($Fo_{82\text{-}89}$) is found in the macrocryst cores of both potassic and ultrapotassic lavas. Forsterite content is lower ($Fo_{71\text{-}81}$) in the rims and some macrocryst cores of potassic lavas.

Nickel content shows a broadly positive correlation with forsterite content in olivine cores at Fo_{82}-Fo_{89} (potassic series, 0.01–0.43 wt % NiO, n = 25; ultrapotassic series, 0.09–0.68 wt % NiO, n = 10) (Fig. 8a). This group is also characterized by lower MnO contents (<0.25 wt %) and slightly lower CaO contents (0.07–0.16 wt % CaO), compared to the olivine rims (potassic series, 0.32–0.45 wt % MnO, 0.13–0.29 wt % CaO, n = 6; ultrapotassic series, 0.36 wt % MnO; 0.16 wt% CaO, n = 1) (Fig. 8b–c).

Most olivine crystals are not in equilibrium with the whole rock (Fig. 8d). The most primitive olivines are cores in both the potassic and ultrapotassic series and, in some cases, show a Mg# exceeding the equilibrium line. The compositions in equilibrium (n = 14) were used to estimate temperatures by using the olivine-melt thermometer (eqn. 21; WFFeo = 0.9; spreadsheet Olivine_and_glass_03_14_18. xls) (Putirka, 2008). For melt composition, we used the corresponding whole-rock composition. Mineral-pairs were checked to ensure they satisfy the equilibrium condition K_D $(Mg–Fe)^{ol\text{-}liq}$ = 0.30 ± 0.03 (Roeder and Emslie, 1970), and yielded temperatures of 1209–1303 °C for 7 kbar (~21 km) in anhydrous conditions. The olivines of potassic lavas gave 1209–1252 °C (n = 10), whereas those of the phlogopite-bearing

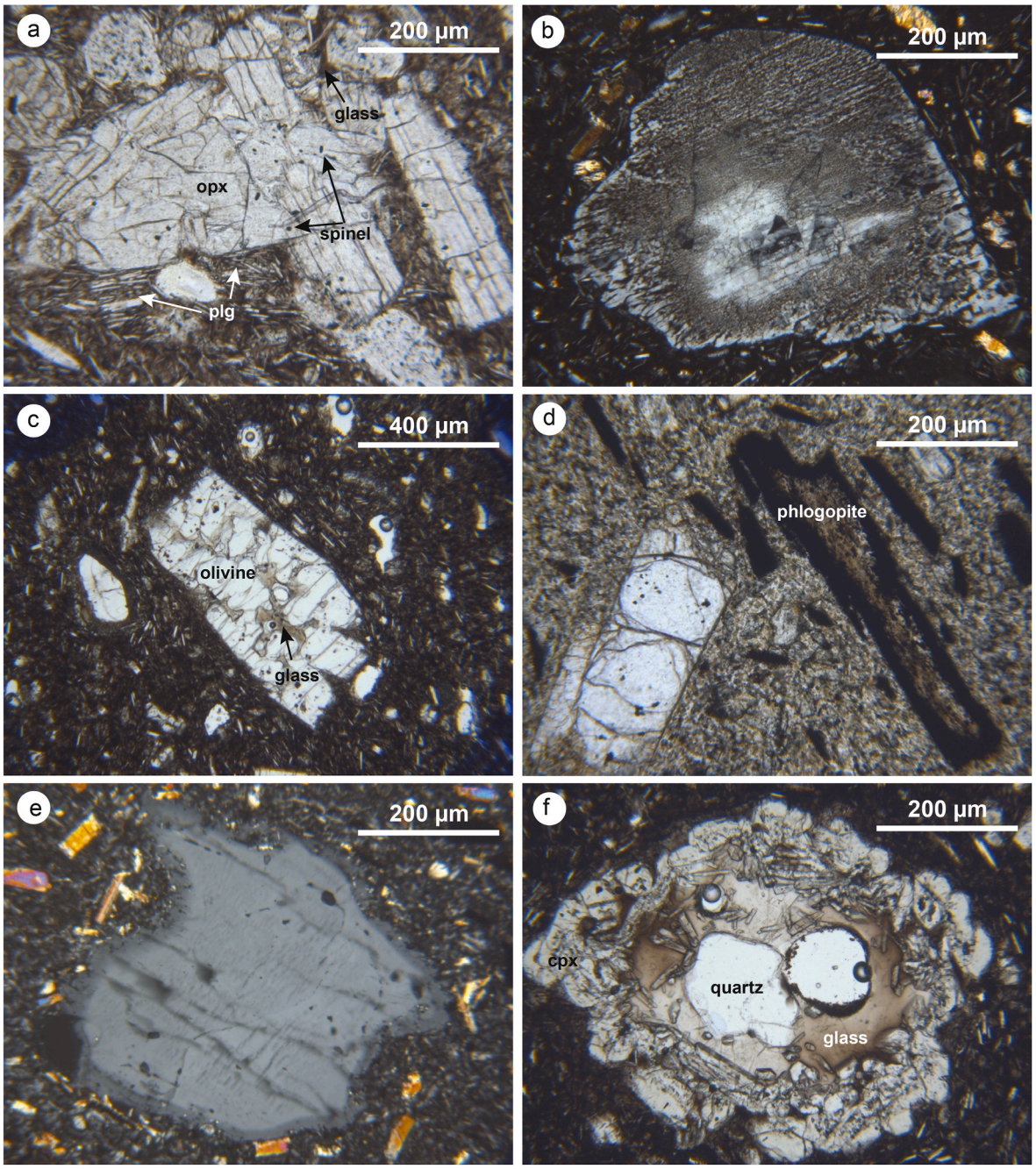

Fig. 4. Photomicrographs (plane-polarized light, PPL; cross-polarized light, CPL) of representative petrographic features of San Jerónimo and Negro de Chorrillos lava flows. (a) Orthopyroxenes (opx) forming a glomeroporphyric texture with inclusions of spinels (sample SJ-5, PPL). (b) Plagioclase with sieve texture defined by a core, a dusty or fritted zone, and a rim (sample SJ-5, CPL). (c) Olivine phenocryst with corrosion gulfs (sample SJ-5, PPL). (d) Phlogopite phenocrysts embayed and rimmed by opaque minerals (NdC-3, PPL). (e) Sanidine xenocryst with anhedral appearance due to the strongly rounded edges of the crystal (NdC-3, CPL). (f) Quartz xenocryst with the corona of glass and clinopyroxene (cpx) (sample SJ-5, PPL).

ultrapotassic compositions reach 1283–1303 °C (n = 4).

4.4.2. *Pyroxenes*

Clinopyroxene macrocrysts, microcrysts, and coronas in SJ and NdC lava flows are classified (Morimoto, 1988) as augite-diopside and, only in SJ, as clinoenstatite. Orthopyroxene macrocrysts are enstatite and were only observed in the SJ potassic series (sample SH-5), forming cumulates. Clinopyroxene macrocrysts (Wo_{33-47} En_{42-53} Fs_{9-14}) and microcrysts (Wo_{40-45} En_{41-49} Fs_{10-16}) of the potassic series define a variation trend from 0.42 to 1.76 wt % TiO_2 and 1.63 to 5.22 wt % Al_2O_3. Despite the textural difference and petrogenetic significance, the composition of coronas (Wo_{38-45} En_{41-52} Fs_{7-15}), from 0.14 to 2.04 wt % TiO_2 and 0.05 to 5.60 wt % Al_2O_3, overlaps those of the macro and microcrysts. Orthopyroxene macrocrysts in this potassic series show high ferromagnesian contents (Wo_{3-9} En_{76-83} Fs_{14-18}) and lower values and narrower ranges for TiO_2 (0.19–0.35 wt %) and Al_2O_3 (1.06–2.52 wt %). In the ultrapotassic series, clinopyroxene macrocrysts (Wo_{39-45} En_{41-52} Fs_{8-15}), microcrysts (Wo_{42-44} En_{46-50} Fs_{8-10}) and coronas (Wo_{42-44} En_{47-50} Fs_{8-11}) overlap the compositions observed in the potassic series, although the variation ranges are narrower for TiO_2 (0.41–1.69 wt %) and Al_2O_3 (0.84–4.07 wt %). Clinopyroxene macrocryst and microcryst compositions are mostly outside the range of crystal-melt equilibrium

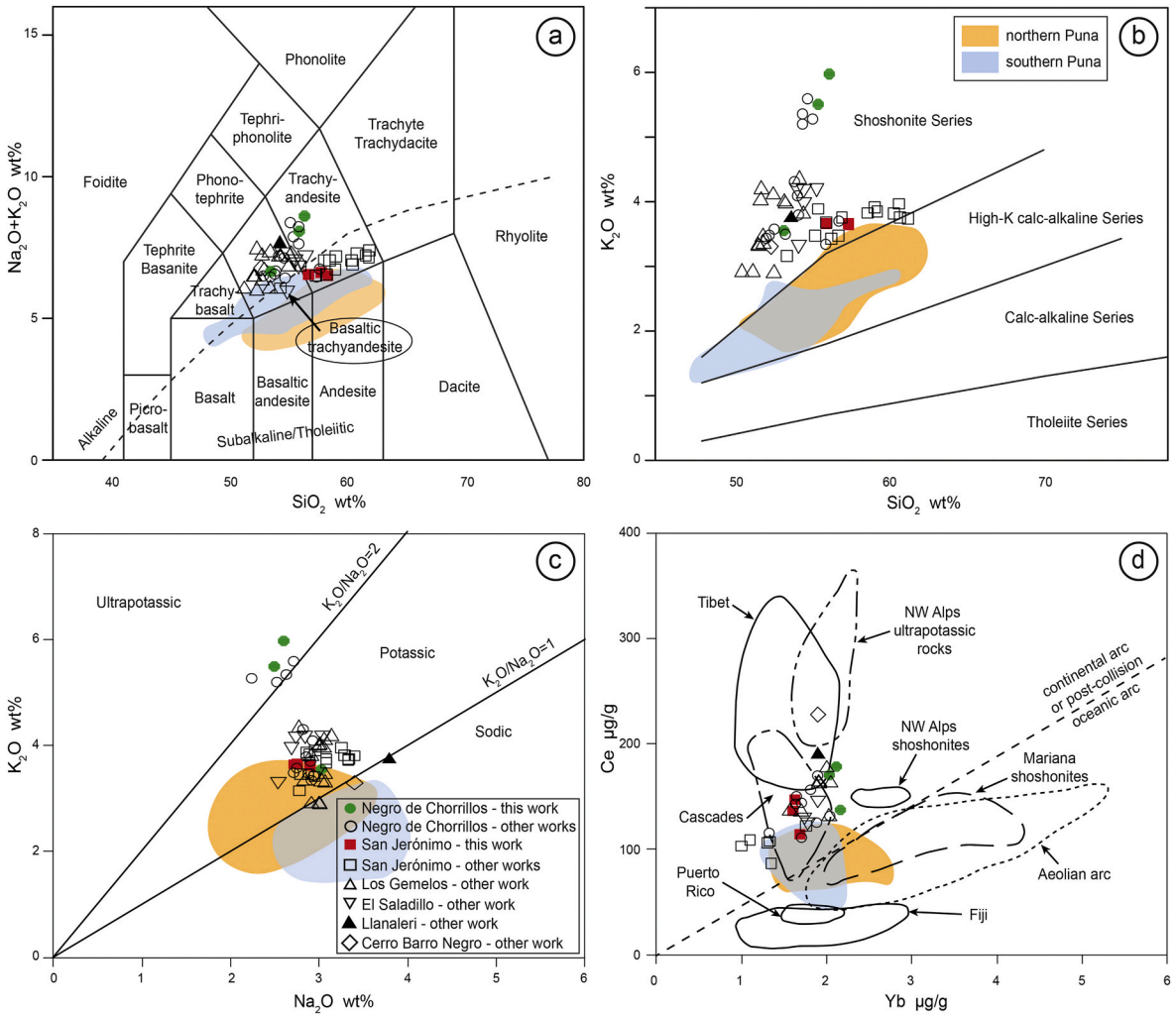

Fig. 5. Composition on anhydrous basis of San Jerónimo and Negro de Chorrillos samples using data of this work and from other studies (Déruelle, 1991; Hörmann et al., 1973; Kay et al., 1994; Krallmann, 1994; Murray et al., 2015; Schreiber and Schwab, 1991), and comparison with the shoshonitic centres of Los Gemelos and El Saladillo (Guzmán et al., 2006; Hausen, 1937; Hörmann et al., 1973; Kay et al., 1994; Krallmann, 1994), Llanaleri (Krallmann, 1994), and Cerro Barro Negro (Maro et al., 2016b). (a) Classification in the Total Alkali-Silica (TAS) diagram (Le Bas et al., 1986) with a dashed line separating the subalkaline from the alkaline field (Irvine and Baragar, 1971). (b) Classification in the SiO_2 vs. K_2O plot (Peccerillo and Taylor, 1976) (Irvine and Baragar, 1971). (c) Na_2O–K_2O classification of potassic and ultrapotassic rocks (MgO > 3 wt %) (Foley et al., 1987; Gill, 2010). (d) Ce–Yb plot showing the studied samples compared with shoshonites fields of several regions with alkaline volcanism worldwide (Gill et al., 2004). The reference of the symbols for all plots is in (c). The compositional fields of the Neogene mafic volcanic rocks of northern Puna (Maro et al., 2016b) and southern Puna (Báez et al., 2017; Drew et al., 2009; Risse et al., 2013) are also indicated as reference.

compositions for potassic and ultrapotassic samples, using an iron-magnesium distribution coefficient of 0.28 ± 0.08 for clinopyroxene (Putirka, 2008) (Fig. 9a). Corona compositions are mostly outside of the equilibrium field, but some are also inside (particularly in sample SJ-1). The P-T conditions for clinopyroxene-liquid equilibrium are sensitive to both temperature and pressure and calculated using an iterative simultaneous solution method (WFFeo = 0.9; anhydrous conditions; spreadsheet Clinopyroxene_P-T_9-26-16. xls) (Putirka, 2008). This geothermobarometer yielded pressure estimates between 7.1 kbar and 0.0 kbar and temperature between 1180 and 1100 °C (Fig. 9b). Pyroxene coronas in the ultrapotassic samples yielded 6-2 kbar, whereas coronas in the potassic samples are in the entire range of calculated pressures.

4.4.3. Phlogopite

Macrocrysts and microcrysts of phlogopite occur only in the ultrapotassic series (Fig. 4d). The composition ($Fe^{2+}/(Fe^{2+}+Mg) < 0.33$; Al^{IV} = 2–3 apfu; n = 8)) classify them as phlogopite (Deer et al., 2013).

4.4.4. Feldspars

The ternary Ab-An-Or diagram for feldspars is shown in Fig. 10. In the potassic series, macrocrysts (core and rim) and microcrysts are mostly within plagioclase solid-solution series, whereas macrocryst dusty zones show compositions between anorthoclase and sanidine solid-solution series close to hotter isotherms (Fuhrman and Lindsley, 1988) (Fig. 10). The cores of these macrocrysts are quite sodic (An_{21-52} Ab_{44-70} Or_{3-25}), while dusty zones are more potassic (An_{11-63} Ab_{32-52} Or_{5-50}), and their overgrowth rims are significantly more calcic (An_{45-70} Ab_{28-48} Or_{2-7}). Microcryst compositions (An_{44-71} Ab_{27-47} Or_{2-14}) overlap the compositions of the last rims.

Conspicuous by its absence is the lack of dusty zones on feldspar macrocrysts of the ultrapotassic series. The core and rim compositions of these macrocrysts and the microcrysts are more frequent within the sanidine and anorthoclase solid-solution series than in the plagioclase solid-solution series. The core compositions of these macrocrysts show a quite potassic trend (An_{0-33} Ab_{21-52} Or_{22-79}), largely overlapping the compositions of the macrocryst rims (An_{5-26} Ab_{28-36} Or_{38-67}) and microcrysts (An_{6-45} Ab_{32-48} Or_{11-62}).

4.4.5. Glass

Glass is more common in the potassic (14.2–37.1 vol %) than in the

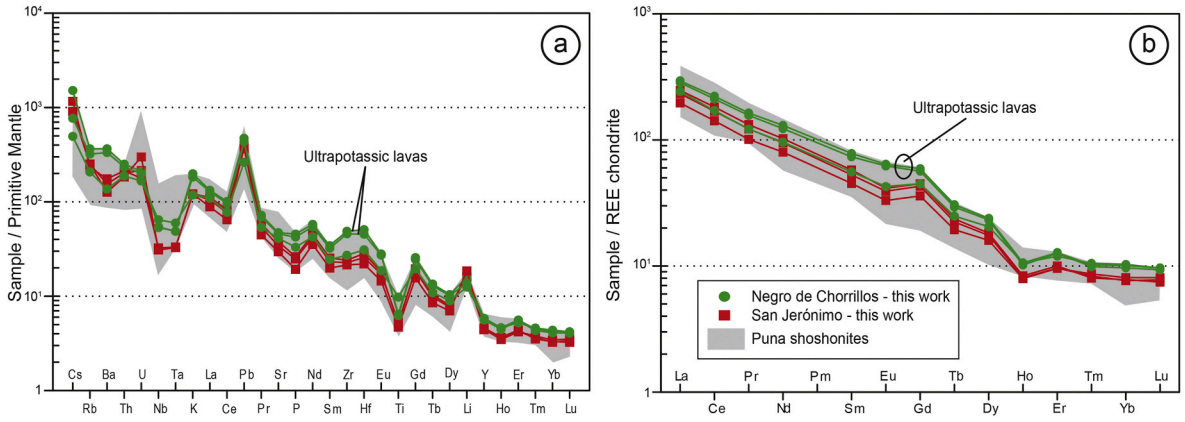

Fig. 6. (a) Spidergram showing incompatible element enrichment patterns relative to the primitive mantle (Sun and McDonough, 1989). (b) Chondrite-normalized (Boynton, 1984) REE patterns. The grey field comprises the compositions of San Jerónimo and Negro de Chorrillos samples using data of this work and from other studies (Déruelle, 1991; Kay et al., 1994; Krallmann, 1994; Murray et al., 2015; Schreiber and Schwab, 1991), the shoshonitic centres of Los Gemelos and El Saladillo (Guzmán et al., 2006; Hausen, 1937; Hörmann et al., 1973; Kay et al., 1994; Krallmann, 1994), Llanaleri (Krallmann, 1994), and Cerro Barro Negro (Maro et al., 2016b).

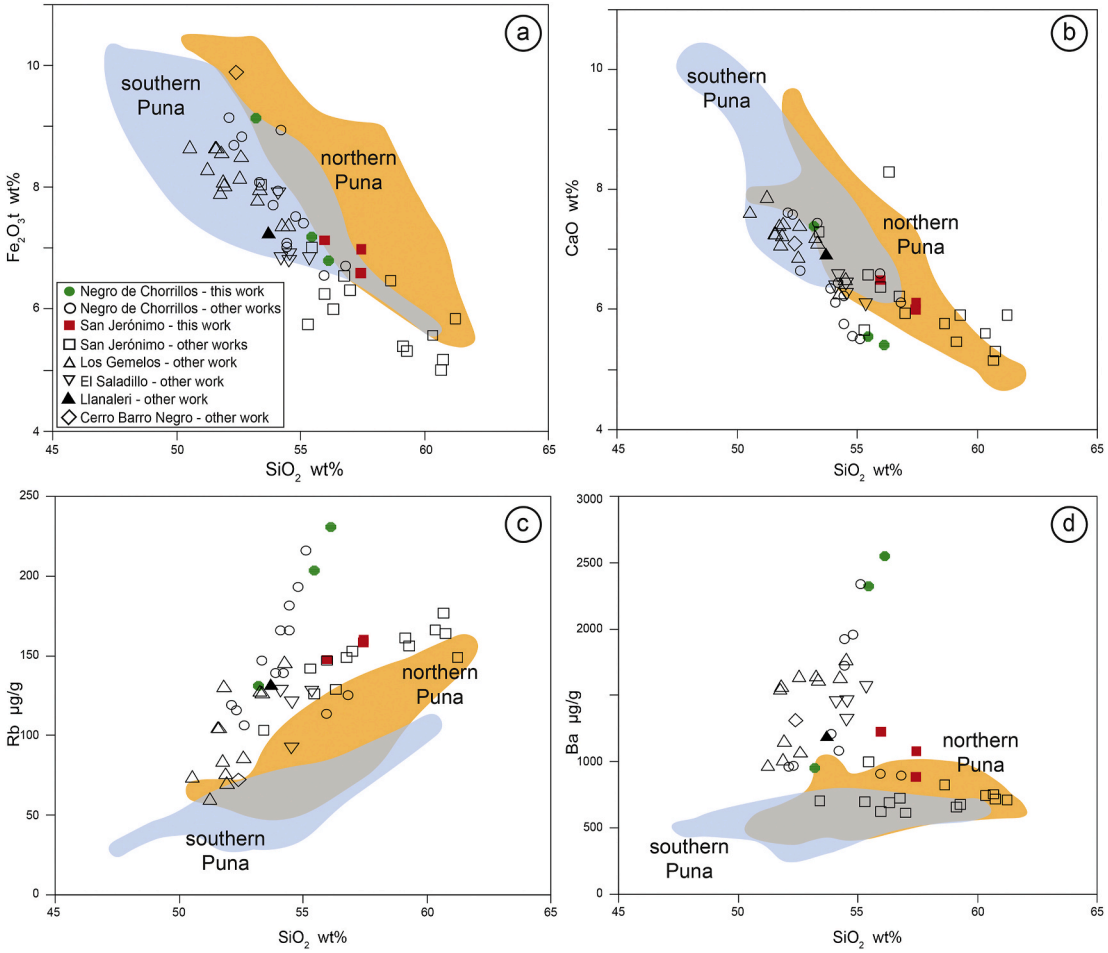

Fig. 7. Selected Harker diagrams of San Jerónimo and Negro de Chorrillos using data of this work and from other studies (Déruelle, 1991; Kay et al., 1994; Krallmann, 1994; Murray et al., 2015; Schreiber and Schwab, 1991), the shoshonitic centres of Los Gemelos and El Saladillo (Guzmán et al., 2006; Hausen, 1937; Hörmann et al., 1973; Kay et al., 1994; Krallmann, 1994), Llanaleri (Krallmann, 1994), and Cerro Barro Negro (Maro et al., 2016b). The compositional fields of the Neogene mafic volcanic rocks of northern Puna (Maro et al., 2016b) and southern Puna (Báez et al., 2017; Drew et al., 2009; Risse et al., 2013) are also indicated as reference.

ultrapotassic (0.4–2.1 vol %, series (Table 2). The glass compositions define two groups in the SJ and NdC lava flows: glasses in the groundmass and glasses in coronas together with clinopyroxene surrounding quartz crystals. There are glass compositions of the potassic series in both groups but only from coronas in the ultrapotassic series, since microanalysis of the interstitial glass in the latter was not possible

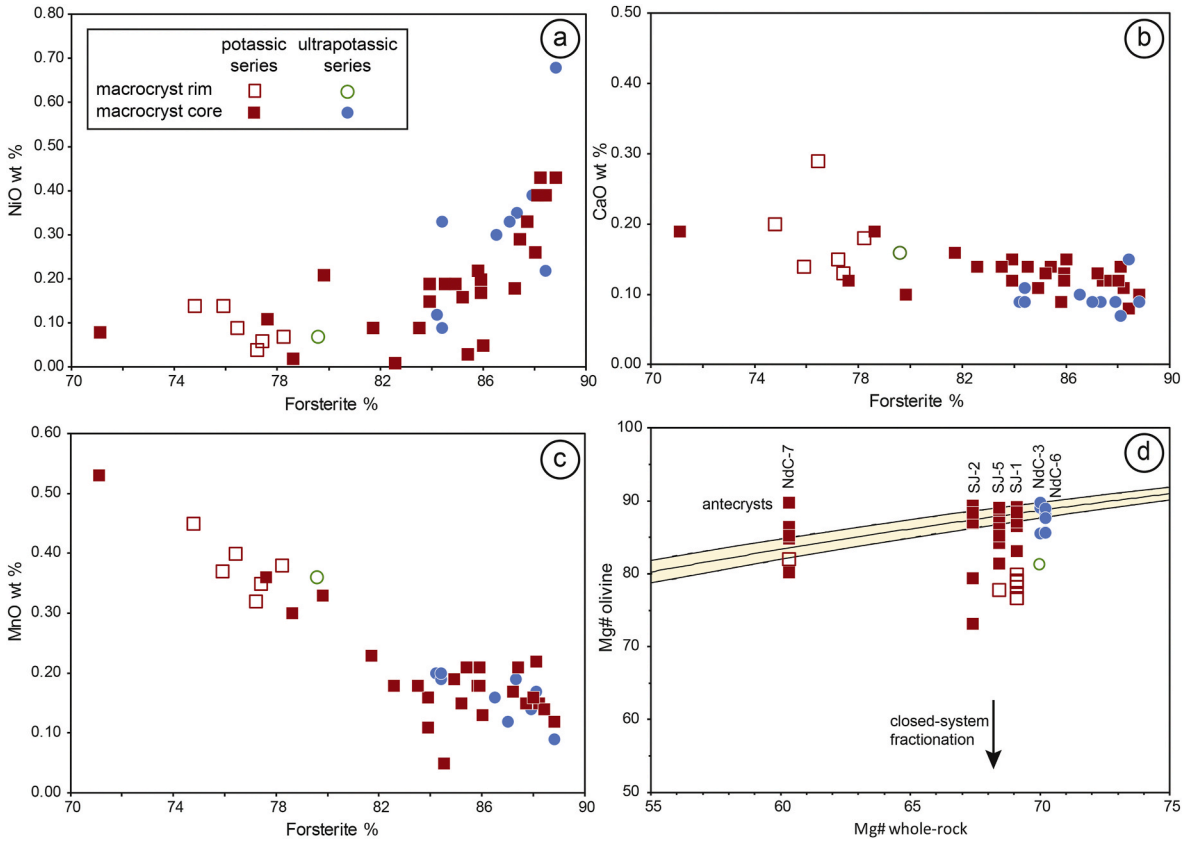

Fig. 8. Forsterite (mol % forsterite component) versus (a) NiO (wt %), (b) CaO (wt %), and (c) MnO (wt %) in olivines from the studied eruptive potassic and ultrapotassic series. Note the change of trend at ~Fo_{82}, a reflection of the bimodality of olivine compositions. Olivine cores display a broadly positive correlation of NiO with forsterite content and a negative correlation with MnO, constituting an olivine-dominated crystallization trend. Instead, olivine compositions from rims show lower forsterite (Fo < 82) and NiO (<0.15 wt %). (d) Rhodes diagram (whole-rock Mg# vs. olivine Mg#) for San Jerónimo and Negro de Chorrillos lava flows. The yellow field represents the range of crystal-liquid equilibrium compositions for K_D $(Mg–Fe)^{ol\text{-}liq} = 0.30 \pm 0.03$ (Roeder and Emslie, 1970).

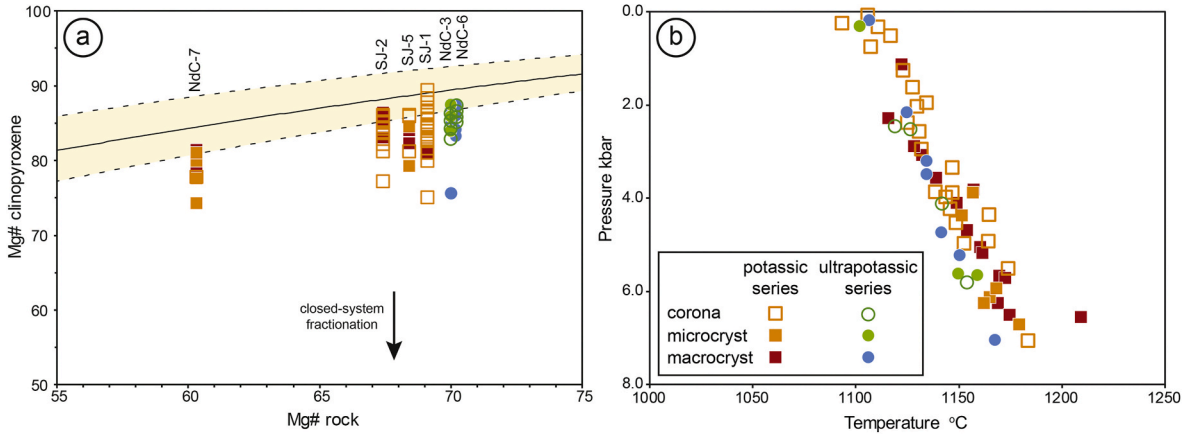

Fig. 9. Mg# in whole-rock vs Mg# in mineral for clinopyroxene of San Jerónimo and Negro de Chorrillos lava flows (a); the yellow field represents the range of crystal-melt equilibrium compositions using an iron-magnesium distribution coefficient of 0.28 ± 0.08 for clinopyroxene (Putirka, 2008). The P-T estimates (b) were calculated by iterative simultaneous solution based on the clinopyroxene-melt equilibrium (Putirka, 2008).

because of their practically fully crystallized groundmass (Fig. 11). The potassic series's interstitial glasses range mainly from basaltic–trachyandesite to the trachyte-trachydacite field in a TAS diagram, reaching even the rhyolitic field (Fig. 11). Instead, the group of corona glasses ranges from trachyte-trachydacite to rhyolitic TAS fields, being all corona glasses of the ultrapotassic series of rhyolitic composition.

4.4.6. *Opaque minerals*

Opaque minerals in the SJ and NdC lava flows are included in olivine, clinopyroxene and orthopyroxene macrocrysts in the potassic series and only in olivine in the ultrapotassic series, as well as microcrysts in the groundmass in both cases. Macrocryst inclusions are mainly Cr-spinel, whereas titanomagnetite occurs as microcrysts in the groundmass. Only in one case, ilmenite was found in the groundmass (SH-1) and, in another case, rutile in apatite (SH-2). In the potassic

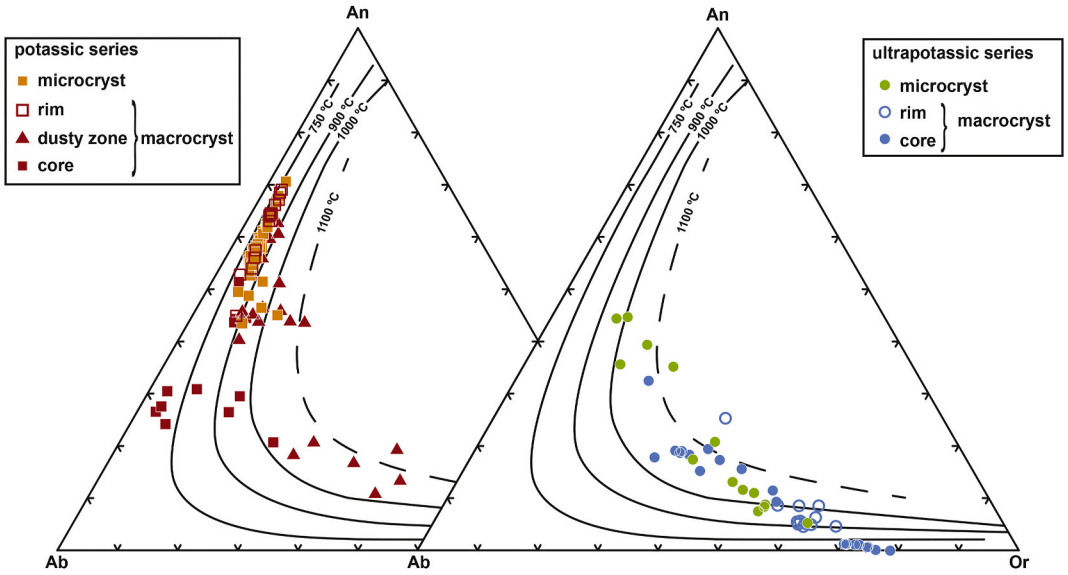

Fig. 10. Compositions of feldspars in the Ab-Or-An diagram. Isotherms for 1 kbar from Fuhrman and Lindsley (1988).

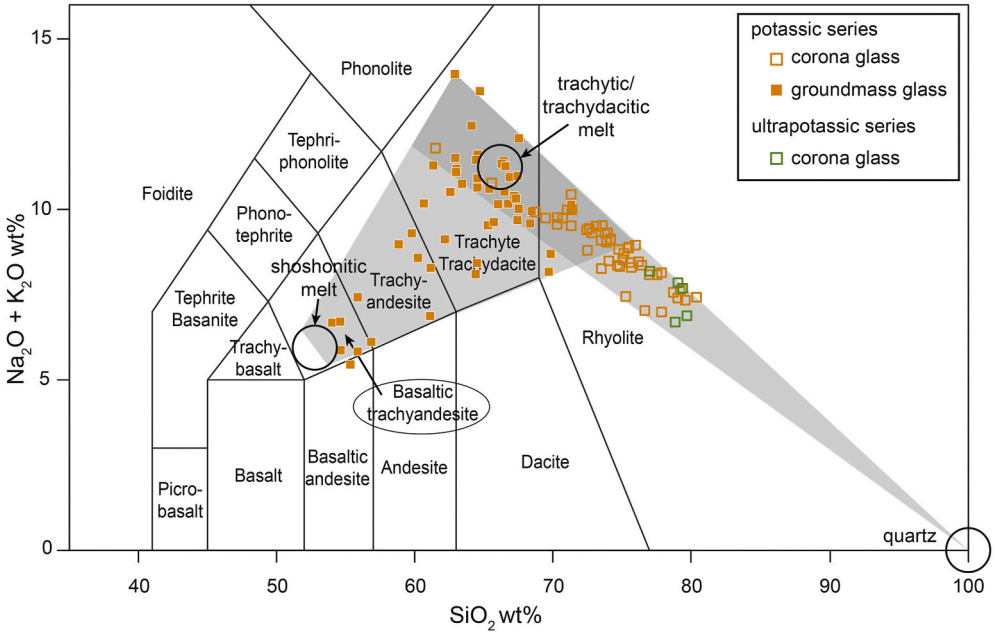

Fig. 11. Total alkalis vs. SiO_2 (TAS) classification diagram (Le Bas et al., 1986) for the interstitial glass in the groundmass and the glasses associated with coronas surrounding quartz crystals. Data are normalized to 100%. The shoshonitic melt, trachytic-trachydacitic melt and quartz end members are reported to explain the glass composition variation. See details in the discussion section.

series, Cr-spinel crystals included in olivine (n = 39) show 1.02–10.95 wt % TiO_2 and chromium numbers from 0.56 to 0.73 (Cr# = Cr/(Cr + Al), mol); those included in clinopyroxene (n = 7) have 1.62–7.09 wt % TiO_2 and Cr# from 0.55 to 0.71, and the composition of one crystal included in orthopyroxene is 2.24 wt % TiO_2 and Cr# of 0.58 (Fig. 12). In the matrix, the composition of titanomagnetites ranges from 3.31 to 17.36 wt % TiO_2. The ilmenite in the matrix has 35.29 wt % TiO_2 (n = 1) and the rutile included in apatite 89.15 wt % TiO_2 (n = 1). In the ultrapotassic series, Cr-spinel crystals included in olivine (n = 12) show 1.45–1.92 wt % TiO_2 and Cr# from 0.74 to 0.80 (Fig. 12). The composition of titanomagnetites ranges from 8.44 to 12.98 wt % TiO_2 (n = 5) in the matrix.

4.5. Geochronology

New K–Ar ages were determined on unaltered groundmass from fresh samples from SJ and NdC lavas. The age determined for sample SJ-2 of San Jerónimo is 144 ± 3 ka (±2σ error) (Table 3). The sample NdC-3 of Negro de Chorrillos provided an age of 51 ± 2 ka (±2σ error) (Table 3).

To help constrain these eruptions temporally within the younger mafic volcanism of the Puna, we also determined the age of the Alumbrera eruption, considered one of the younger volcanoes of the region due to its well-preserved landforms (scoria cone and lava flows). The sample CB3001-D of a lava flow of the Alumbrera volcanic centre provided an age of 37 ± 2 ka (±2σ error) (Table 3).

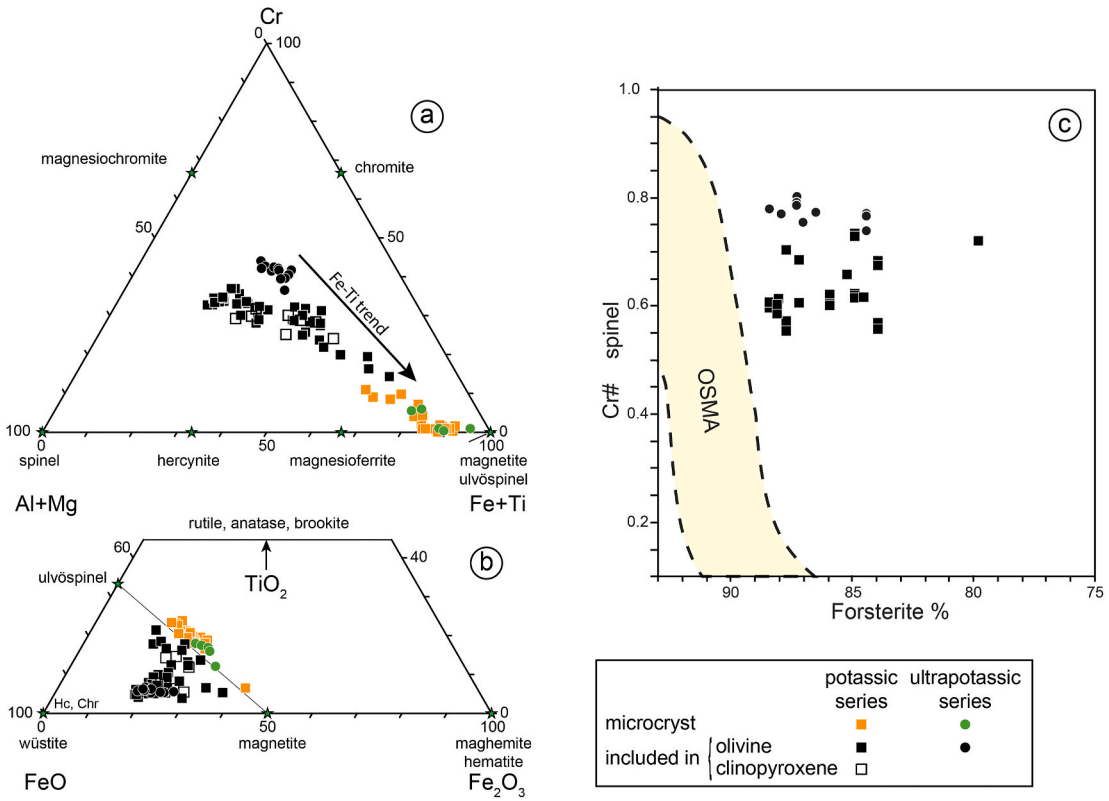

Fig. 12. Spinel compositions in the potassic and ultrapotassic series of the San Jerónimo and Negro de Chorrillos lava flows. (a) Spinel (Al + Mg)–Cr-(Fe + Ti) ternary diagram; arrow denotes the Fe–Ti variation trend of spinel compositions, along which Fe^{3+}, $Fe^{2+}/(Mg + Fe^{2+})$ and TiO_2 increase at constant Cr/(Cr + Al) (Barnes and Roeder, 2001). (b) FeO–TiO_2–Fe_2O_3 ternary diagram for spinels. (c) Relationship between the content of forsterite in olivine and Cr# of spinels enclosed in this mineral; OSMA, olivine-spinel mantle array (Arai, 1994).

Table 3
K–Ar ages of samples from the shoshonitic volcanoes of San Jerónimo and Negro de Chorrillos and the basaltic andesite Alumbrera volcano, one of younger mafic eruptions of the Puna. Age calculations are based on the decay and abundance constants from Steiger and Jager (1977). Errors on the age include the 1% uncertainty on the $^{40}Ar^*$ content of the calibration standards.

SAMPLE Experiment	M. P.	K (wt%) ± 1σ	Mass molten (g)	$^{40}Ar^*$(%)	$^{40}Ar^*10^{-13}$ (mol/g) ± 1σ	Weighted mean $^{40}Ar^*10^{-13}$ (mol/g) ± 1σ	Age ka ± 2σ
CB3001-D							
IGSN IEJLF001Z							
8674	(+)	2.225 ± 0.022	2.00294	0.784	0.139 ± 0.058	0.143 ± 0.049	37 ± 2
8698			1.94134	1.855	0.151 ± 0.089		
NdC-3							
IGSN IEJLF001W							
8586	(+)	5.105 ± 0.151	1.01915	1.041	4.310 ± 0.167	4.486 ± 0.113	51 ± 2
8602			1.02974	1.855	4.633 ± 0.154		
SJ-2							
IGSN IEJLF001U							
8585	(+)	3.188 ± 0.032	1.04809	2.894	7.964 ± 0.198	7.946 ± 0.109	144 ± 3
8601			1.00288	2.891	7.939 ± 0.130		

M. P. Magnetic polarity, (+) normal polarity.

5. Discussion

5.1. Morphometry

SJ and NdC eruptions produced Strombolian scoria cones and lava flows, the most common expression of the monogenetic volcanism in the Puna (Grosse et al., 2020; Haag et al., 2019). Tephra fallout deposits and pyroclastic flows are rare in this kind of volcanism. However, up to 10 cm thick ash-fall deposits identified in fluvial terraces were associated with the SJ eruption (Kay et al., 2008), and pyroclastic flows and ash fallout were related to the NdC eruption (Seggiaro et al., 2016).

Some morphometric parameters (cone height, h; cone major axis, a_{co}, crater major axis, a_{cr}; flank slope) and some geometrical aspect ratios (h/a_{co} and a_{cr}/a_{co}) are commonly used to compare cinder cones. When compared to the Puna cinder cones (Haag et al., 2019), the cone heights of SJ (258 m) and NdC (162 m) are larger than the mean value (40 m). Their cone major axes (1846 and 1188 m for SJ and NdC) also exceed the mean (400 m). On the other hand, an ideal cinder cone is defined as having $h/a_{co} = 0.18$, $a_{cr}/a_{co} = 0.40$ and a flank slope of ~31° (Fornaciai et al., 2012). Both SJ and NdC h/a_{co} ratios are 0.14, whereas the a_{cr}/a_{co} ratio is 0.08 in SJ and 0.38 in NdC, and the slope median is 20° for the two edifices. The SJ edifice's strong deviation from an ideal

cone is because the SJ edifice is a multiple cone with three main craters (Figs. 2–3).

Lava flows of SJ and NdC have a fresh appearance showing well-preserved structures (levees, lobes, etc.). The maximum lengths reached by these flows (9.4 and 4.5 km for SJ and NdC, respectively) are in the range of 1–14 km observed in the southern Puna's mafic centres (Grosse et al., 2020). The maximum thicknesses of SJ and NdC (20 and 30 m, respectively) are in the high part of the average thicknesses (2–28 m) of these centres' lava flows. The southern Puna's lava flows cover areas between 0.6 and 44 km^2, whereas lava Flows of SJ and NdC covered 8.8 and 4.6 km^2, respectively.

The bulk and DRE volumes of cones are 0.118 and 0.030 km^3 for SJ and 0.034 and 0.009 km^3 for NdC. Compared with cone bulk volumes of the southern Puna ranging between 0.004 and 0.17 km^3 (mean = 0.05 km^3) (Grosse et al., 2020), the SJ cone is among the larger, whereas the NdC cone is close to the average. The bulk and DRE volumes of lava flows are 0.081 and 0.061 km^3 for SJ, and 0.015 and 0.011 km^3 for NdC. Compared with the southern Puna's lava flows, where bulk volumes are between 0.004 and 1.5 km^3 (mean = 0.2 km^3) (Grosse et al., 2020), SJ and NdC lava flow bulk volumes are among the lower values. Finally, the SJ and NdC whole centres (edifice plus lava flows) cover an area of 10.7 and 5.3 km^2, respectively. These values are between 0.1 and 44 km^2, the range observed for mafic centres in the southern Puna (Grosse et al., 2020).

The morphometric differences of monogenetic landforms result from eruption dynamics, pre-eruptive topography, and erosion processes (Di Traglia et al., 2014; Kereszturi et al., 2012; Rodriguez-Gonzalez et al, 2011, 2012). In the case of SJ and NdC, there are contrasts in the pre-eruptive surface slope with median values of 8 and 16°, respectively, and the larger time of exposition to erosion (144 ± 3 ka for SJ against 51 ± 2 ka for NdC). However, the main factor determining the SJ and NdC cones' distinctive morphometries was the eruption dynamics. The three craters of the SJ edifice indicate a complex eruptive history with shifts in vent location, whereas a breaching event characterises the NdC edifice morphology.

In summary, SJ and NdC eruptions produced scoria cones, lava flows and practically imperceptible pyroclastic fall deposits resulting from a Strombolian-type eruption with a Volcanic Explosivity Index (VEI) of 2 (Newhall and Self, 1982).

5.2. Petrography

Three of the most remarkable petrographic features of the studied samples are the presence of phlogopite in some lava flows, the mismatch of mineral assemblages (co-occurrence of olivine and quartz, the latter considered as xenocryst), and the common occurrence of disequilibrium textures. We have not observed phlogopite in SJ's longest lava flow (samples SJ-1, SJ-2, SJ-5; Table 2), although this mineral was previously referred at SJ volcano (Déruelle, 1991). Concerning the NdC eruption, Urquizo Furlán (2012) identified three eruptive phases, and we have observed phlogopite in the second phase (samples NdC-3, NdC-6; Table 2). Sample NdC 7 corresponds to a lava flow of the third phase without phlogopite. Thus, both eruptions had phases that erupted products with and without phlogopite.

Common examples of disequilibrium crystal textures are the sieve and dusty textures in plagioclase macrocrysts, where pervasive resorption may affect the entire crystal leading from a microscopic sieve texture (Stewart and Pearce, 2004) to a dusty texture consisting in a nebula of nearly sub-microscopic glass droplets (Tsuchiyama, 1985). The dusty texture (Fig. 4b) may be related to magma mixing, where preexisting sodic plagioclase is suddenly exposed to hotter, more mafic conditions (e.g., with more Ca), thereby reacting and dissolving to produce dusty rims (Hibbard, 1981; Kawamoto, 1992; Richer et al., 2004; Tsuchiyama, 1985; Viccaro et al., 2010). The thickness of the reaction rim is proportional to the duration of heating (Tsuchiyama, 1985).

Other disequilibrium crystal textures are due to peripheral dissolution and may range from subtle rounding of crystal edges to strongly rounded or embayed crystals. This process affected feldspars (Fig. 4e), olivine (Fig. 4c) and pyroxenes. Replacement reactions because of disequilibrium result in rims of opaque minerals around phlogopite phenocrysts (Fig. 4d) and the occurrence of coronas of clinopyroxene (augite) and glass around quartz xenocrysts (Fig. 4f). The latter feature is relatively common in the Puna back-arc mafic rocks (Coira and Kay, 1993; Maro et al., 2017; Risse et al., 2013) and evidences the quartz's reaction with mafic melt (Sato, 1975).

5.3. Whole-rock geochemistry

The sample compositions presented in this work overlap the previously reported data for SJ and NdC in the TAS diagram (Fig. 5a), classifying all considered samples as basaltic trachyandesites and trachyandesites. The shoshonitic assignment of SJ and NdC lava flows (Fig. 5b) was described in previous works (Déruelle, 1982, 1991; Ducea et al., 2013; Knox et al., 1989; Murray et al., 2015; Schreiber and Schwab, 1991). Considering the grouping in potassic and ultrapotassic rocks (Fig. 5c) the total dataset contains five ultrapotassic samples, all from NdC (Déruelle, 1991; Kay et al., 1994; Murray et al., 2015). The occurrence of phlogopite phenocrysts in these samples is confirmed in three cases, two in this work (Table 2) and one from Déruelle (1991; N16W). Their projection in the Yb–Ce plot indicates a continental magmatic arc setting, close to the Cascades shoshonites from the western USA (Gill et al., 2004) (Fig. 5d).

The shoshonites are distinct from the high-K calc-alkaline volcanic mafic rocks of the northern and southern Puna in their higher K and LILE concentrations, except for Cs (Fig. 6a). The negative anomalies of Nb, Ta and Ti also occur in the mafic rocks of the Puna. This pattern is common in arc magmas, and it is widely believed that it is the geochemical signature of peridotites metasomatized by LILE-LREE-bearing hydrous fluids in the mantle wedge above a subduction zone (Baier et al., 2008; Gill, 2010). In this setting, the negative Nb and Ta anomalies must be related to the very low solubility of Nb and Ta in aqueous fluids and the high solubility of these elements in aluminous clinopyroxene, rutile, and potentially some other phases, under relatively low pressures (10–20 kbar) in the shallow part of the subduction zone (Baier et al., 2008). Concerning the positive anomalies, Pb provides evidence for crustal assimilation. On the other hand, the enrichment in Li in Neogene volcanic rocks of CVZ is due to the combination of Palaeozoic basement assimilation with the mantle-derived signature (Meixner et al., 2020).

SJ and NdC samples show low Ba/Rb (5.6–11.4) and high Rb/Sr (0.1–0.2) ratios, typical ranges for lavas derived from phlogopite-bearing sources because Rb and Ba are compatible in phlogopite, whilst Rb, Sr and Ba are moderately compatible in amphibole (Wei et al., 2017). The enriched LREE patterns may be related to a thick continental crust (Winter 2010), while the flat heavy REE (HREE) tail suggests a garnet-free source, implying relatively shallow depths of magma formation in the upper mantle (Davidson et al., 2007a; Winter 2010). The lack of a significant Eu anomaly (Eu/Eu*, 0.81 to 0.97) suggests that plagioclase is not a major phase involved in fractional crystallization processes.

5.4. Mineral and glass compositions

5.4.1. Olivine

The compositional variations of NiO, CaO and MnO (Fig. 8a–c) as a function of forsterite indicate that the olivine macrocrysts crystallized from a compositionally related suite of magmas and are not xenocrysts from the mantle or other sources. With rising of forsterite, the slight fall in CaO agrees with experimental works explaining that both the forsterite content of the olivine and the magma CaO content are major controls on CaO in olivine (Libourel, 1999; Thompson and Gibson, 2000). Furthermore, CaO and forsterite contents are higher than those of

typical mantle xenocrysts (Liu et al., 2011; Straub et al., 2011; Thompson and Gibson, 2000). Besides, in both the potassic and ultrapotassic series, some olivine cores show a Mg# exceeding the equilibrium line, suggesting that they are antecrysts (Davidson et al., 2007b; Larrea et al., 2014) (Fig. 8d). Instead, the olivines with Mg# under the equilibrium line evidence fractionation processes in a closed system. These features support the hypothesis that all analysed olivines are magmatic and not from mantle sources. Finally, the evolution trend defined by lower values of forsterite (Fo < 82, Fig. 8a–c) is consistent with a lower temperature and pressure crystallization, i.e., the rims crystallized at lower temperature and pressure compared to the cores. In these conditions, plagioclase and clinopyroxene co-crystallized with olivine. Crystallization of plagioclase at high crustal levels increases the CaO/Al_2O_3 ratio and alkalis ($Na_2O + K_2O$) content in the melt favouring the Ca incorporation in olivine rims (Libourel, 1999).

5.4.2. Pyroxenes

In both the potassic and ultrapotassic lavas, the compositions of clinopyroxene macrocrysts and microcrysts are mainly outside the crystal-melt equilibrium compositional range (Putirka, 2008) (Fig. 9a). This supports that these clinopyroxenes are the product of fractionation processes. The corona compositions are also mostly outside of the equilibrium field, but their texture demonstrates quartz xenocrysts' reaction with mafic melt (Sato, 1975).

The wide range obtained for pressure (up to 7.1 kbar, up to ~21.3 km) and the narrow range of temperature (1180–1100 °C) suggest a fast ascent rate (Fig. 9b). While the pyroxene coronas in the ultrapotassic lavas formed between 6 and 2 kbar, the coronas of the potassic lavas grew between 7.1 kbar and the surface. Clinopyroxene temperatures are ~30–~200 °C lower than those obtained for olivine (1209–1303 °C). This feature is interpreted as a consequence of clinopyroxene crystallizing after olivine, although no petrographic evidence supports this.

5.4.3. Phlogopite

The wide compositional variation in TiO_2 (2.89–8.85 wt %) and FeOt (5.14–9.53 wt %) in macrocrysts of phlogopite allows us to interpret them as phenocrysts, which are liquidus and near-liquidus phases, excluding their origin as mantle xenocrysts (Fritschle et al., 2013). The high Mg# (0.77–0.89) of phlogopites and their host rocks (0.70) indicate a deep origin, i.e., high P-T conditions in the range of 20–50 km depth for temperatures of 1100–1200 °C (Condamine and Médard, 2014; Gill, 2010). In this context, our magmas would be generated at the highest depth of spinel lherzolite's stability field (40–50 km). On its ascent and up to a depth of about 20 km, the phlogopite would form.

5.4.4. Feldspars

Dusty feldspar macrocrysts (Fig. 4b) are suggested to have formed by resorption of relatively albitic plagioclase xenocrysts due to the influx of the more calcic shoshonitic magma. Subsequently, more An-rich plagioclase crystallized from the hybrid host to form the thin high-calcium outermost rim. The occurrence of K-feldspar in phlogopite-bearing rocks results from the equilibria that include phlogopite, either with olivine or with pyroxene, where the potassium of phlogopite will remain as sanidine (Deer et al., 2013).

5.4.5. Glass

The wide range of compositional variation in glasses (Fig. 11) also evidences the mixing of magmas. We observe two compositional trends of glasses. The trend of groundmass glasses may result from both hybridization of melts and fractionation. Hybridization is represented by samples of the potassic series, with a high glass content (14–37%). Similar trends were observed in groundmass glasses of the Grizzly Lake complex of Yellowstone Volcano and were interpreted as the hybridization of mafic and felsic magmas (Morgavi et al., 2016). Instead, fractionation leads to rocks with low contents of more primitive interstitial glass (0–2%), i.e., samples of the ultrapotassic series. The second compositional trend corresponds to glasses of coronas around quartz xenocrysts (Fig. 11). In the potassic series, there was a large quantity of melt to react and the result was a wide range of compositions. However, in the ultrapotassic series, the melt was scarce and more evolved, resulting in a silica-rich glass. The two before mentioned compositional trends of glasses converge in the trachyte-trachydacite field of the TAS diagram (Fig. 11), i.e., the composition of the felsic end-member involved in the mixing process. This composition is not uncommon in the region. Ignimbrites of the Puna have a composition similar to the postulated trachyte-trachydacite composition of these felsic melts (Murray et al., 2015).

5.4.6. Opaque minerals

The compositions of Cr-spinels and titanomagnetites in a ternary plot of (Al + Mg)–Cr-(Fe + Ti) (Fig. 12a) show that the potassic and ultrapotassic series follow the Fe–Ti variation trend of spinel compositions, along which Fe^{3+}, $Fe^{2+}/(Mg + Fe^{2+})$ and TiO_2 increase at constant Cr/(Cr + Al) (Barnes and Roeder, 2001). However, the Cr content is slightly higher in the spinels enclosed in the ultrapotassic series's olivines (Fig. 12b–c). On the other hand, the compositions of Cr-spinels enclosed in olivine (i.e., forsterite content in olivine vs. Cr# of spinels) plot outside the olivine-spinel mantle array (OSMA) (Fig. 12c) (Arai, 1994).

5.5. Geochronology

The new groundmass K–Ar ages of San Jerónimo (144 ± 3 ka) and Negro de Chorrillos (51 ± 2 ka) confirm that NdC is younger than SJ, but both ages are significantly younger than those published before. San Jerónimo volcano was previously dated at 0.78 ± 0.10 Ma (Aquater, 1979; in Coira and Paris, 1981; Linares and Gonzalez, 1990), and Negro de Chorrillos three times with resulting ages of 0.45 ± 0.10 Ma (Linares and Gonzalez, 1990; the original reference is missing in the reference list of this catalogue of ages), 0.20 ± 0.15 Ma (Schwab and Lippolt, 1974), and 0.20 ± 0.08 Ma (Aquater, 1980; in Coira and Paris, 1981; Linares and Gonzalez, 1990). The new ages are younger because the previous ages were obtained from whole-rock while the groundmass provided the new ones. Potassium from older feldspar xenocrysts can cause older whole-rock ages.

The new ages of San Jerónimo and Negro de Chorrillos volcanoes are not enough to decipher the association of pyroclastic density currents (Chorrillos section) and also of reworked ash deposits interbedded in alluvial fans (Corte Blanco section) that have been associated with Negro de Chorrillos volcano (Seggiaro et al., 2016). Lava flows of San Jerónimo eroded the former primary deposits. This fact leads Seggiaro et al. (2016) (p. 475) to deduce that the San Jerónimo volcano had eruptive pulses before and after the Negro de Chorrillos eruption. Dating results confirm the relative chronology between the two eruptions and leave open the discussion about the origin of both deposits. Tentatively, we advance the hypothesis that pyroclastic flows could be related to an unknown eruption before San Jerónimo and Negro de Chorrillos eruptions, while the reworked basaltic ashes east of San Antonio de los Cobres village must be associated with an eruption of greater explosivity than those of SJ and NdC. In the area studied, if the discussed section is of Upper Quaternary age, the most probable candidate is the Tuzgle volcano (Fig. 1), which is located 30 km NW of this section.

Considering the shoshonitic eruptive centres of the Puna, the Cerro Barro Negro is possibly the oldest event recognized because its products are above ignimbrites of 6.4–6.6 Ma (Maro and Caffe, 2013, 2016). Among the young shoshonitic volcanoes, San Jerónimo is the oldest (144 ± 3 ka), followed by Negro de Chorrillos (51 ± 2 ka), and Los Gemelos volcanoes that were formed at around 35 ka, as inferred from the age of lacustrine sediments overlying the lava flows (Guzmán et al., 2006). The age of El Saladillo is unknown.

Although there are still many undated mafic volcanic centres in the Puna, existing data suggest that this activity was restricted in the northern Puna to the Late Miocene-Pliocene interval, with a probable

peak in the Late Miocene (Maro and Caffe, 2016). Instead, the peaks of mafic activity were at 5–4, 3–1 and <1 Ma in the southern Puna (Grosse et al., 2020; Risse et al., 2008; Schoenbohm and Carrapa, 2015), where this monogenetic volcanism is particularly abundant (Grosse et al., 2020). This temporal displacement of the back-arc mafic volcanism from north to south is interpreted as a result of variations in the geodynamic setting, changing slab dips and delamination of the thickened lower crust and lithosphere (Kay and Coira, 2009; Maro and Caffe, 2016).

The excellent preservation of geological formations and structures is a noteworthy characteristic of the Puna due to its aridity (Aulinas et al., 2015). This feature gives a fresh appearance to many recent mafic volcanic edifices suggesting a Late Quaternary age, including Holocene (Báez et al., 2017; Déruelle, 1991). In this framework are the young shoshonitic volcanoes, but also the mafic centres along the western margin of the Arizaro Salar with ages of 0.08–0.22 Ma (Schoenbohm and Carrapa, 2015), the Peinado region with ages of 0.151–0.215 Ma (Grosse et al., 2020), and the region north of Antofagasta de la Sierra with ages of 0.03 and 0.34 Ma (Risse et al., 2008). The Alumbrera Volcano (37 ± 2 ka), located south of this town, is one of the younger basaltic andesite eruptions recorded. In summary, the mafic volcanism of the Puna shows a low recurrence at the Human time scale (Báez et al., 2017; Grosse et al., 2020; Maro et al., 2016b; Risse et al., 2013, 2008).

5.6. Petrogenesis

The long-held hypothesis on the origin of back-arc mafic magmatism in the Puna, including the shoshonitic volcanism, suggest that it is the result of partial melting in the mantle as a consequence of continental lithospheric delamination or foundering (Beck et al., 2015; Coira et al., 1993; de Silva and Kay, 2018; Heit et al., 2014; Kay and Mahlburg Kay, 1993; Kay et al., 1994; Maro et al., 2016b; Murray et al., 2015). This model is supported by seismic tomography images of the mantle wedge (Bianchi et al., 2013; Calixto et al., 2013; Delph et al., 2017; Ibarra et al., 2019; Liang et al., 2014; Mulcahy et al., 2014; Schurr et al., 2006) and by thermomechanical modelling (Sobolev and Babeyko, 2005). It should be noted that only a very minor part of this magmatism is shoshonitic (Maro et al., 2017).

The primitive mantle-normalized incompatible element ratio diagram shows high enrichment in large-ion lithophile elements (LILE, e.g., Rb, Ba, Th, and K), with remarkable depletion in high field-strength elements (HFSE, e.g., Nb, P, Ti) in the studied shoshonites (Fig. 6a). This pattern is similar for the high-K calc-alkaline mafic rocks of the Puna, showing the latter higher K and LILE concentrations, except for Cs. The metasomatism of peridotites can explain this pattern by LILE-LREE-bearing hydrous fluids in the mantle wedge above a subduction zone (Baier et al., 2008; Gill, 2010). On the other hand, flat HREE-Y pattern (normalized to primitive mantle) evidences a spinel lherzolite as the mantle source in this scenario, i.e., a source without garnet (Bédard, 2005; Gill, 2010; Green et al., 2000; LaTourrette et al., 1995; Sun and Liang, 2013; Zhang et al., 2019) (Fig. 6b). This model disagrees with the pyroxenitic source (±garnet–bearing) interpreted previously (Ducea et al., 2013; Murray et al., 2015) and precludes other models based on garnet peridotite (Coira and Kay, 1993; Kay et al., 1994; Knox et al., 1989). Spinel lherzolite is stable at a lesser depth in the mantle than garnet lherzolite, in the range of 20–50 km depth for temperatures of 1100–1200 °C (Condamine and Médard, 2014; Gill, 2010). Based on the crustal thickness of this part of the Puna and the experimental constraint, these magmas last equilibrated at Moho depths at around 50 km (the highest depth of spinel lherzolite stability field). Besides, considering concentrations of 0.05 wt % K_2O and 0.07 wt % TiO_2 for continental spinel lherzolite average (Maaløe and Aoki, 1977), the K_2O/TiO_2 ratio normalized to source composition for shoshonitic samples ranges between 2.23 and 6.81 (n = 49), which indicates a percentage of partial melting lower than 5% (Hirschmann et al., 1999). This threshold of 5% is only exceeded for some samples of shoshonitic mafic centres of the northern and southern Puna.

There is no simple way to explain the transition from primary melts generated in the mantle wedge to shoshonitic magmas. One way can be through the interaction of mantle-derived magma with felsic lower crustal rocks to produce evolved shoshonitic compositions (Richards et al., 2006). Another possibility could be the transition from calc-alkaline to shoshonitic magma compositions due to a general increase of magmatic temperatures and a decrease of H_2O activity (aH_2O) in response to extensional tectonics and related increase of heat flow and declining influence of slab-derived fluids (Beermann et al., 2017). Experimental works point out the feasibility to obtain trachytic melts from K-rich basaltic andesites, the latter formed by melting of a metasomatized phlogopite-bearing mantle in the spinel stability field (Condamine and Médard, 2014). A mantle source consisting of mica-bearing peridotite was already proposed by Déruelle (1991). It should be noted that there is no evidence of mantle phlogopite, spinel, or any other phase of this origin in the samples studied. In any case, the mantle-derived magma evolved and was modified by later processes within the crust, something on which all models of mafic magmatism of the Puna agree (Coira et al., 1993; Déruelle, 1991; Guzmán et al., 2006; Knox et al., 1989; Maro et al., 2017; Risse et al., 2013).

Geochemical data of SJ and NdC shoshonites suggest the development of fractional crystallization processes and the interaction of the shoshonitic melts with others more evolved during the ascent to the surface. Fractional crystallization trends are evidenced by Harker diagrams showing negative correlations of FeO_t (Fig. 7a), MgO, CaO (Fig. 7b), and TiO_2 with SiO_2. However, Al_2O_3, Na_2O, K_2O (Fig. 5b) and P_2O_5 plot in poorly defined trends possibly due to mixing with a more felsic magma. The variations in trace elements also suggest a combination of fractional crystallization and magma mixing to explain the observed variations. For example, Rb and Ba trends show complex variations with SiO_2, the most evolved terms coinciding with the phlogopite-bearing lavas (Fig. 7c–d). Thus, despite the mafic lavas being affected by mixing with more felsic melts, bulk rock geochemistry supports that the lavas with phlogopite represent the most evolved terms reached by fractional crystallization within the mafic melts. This fractional crystallization is coherent with Rb and Ba's partition coefficients for phlogopite (LaTourrette et al., 1995). Similar behaviours are observed for P_2O_5 and Zr variations against SiO_2, in these cases associated with the crystallization of apatite and zircon, respectively.

Fig. 13 presents published Pb, Sr and Nd isotope data of shoshonitic rocks of the Puna (Déruelle, 1991; Guzmán et al., 2006; Kay et al., 1994; Maro et al., 2017; Murray et al., 2015), shown relative to other mafic volcanic rocks of the northern and southern Puna (Drew et al., 2009; Kay et al., 2010; Krallmann, 1994; Maro et al., 2016b; Murray et al., 2015; Risse et al., 2013). The $^{206}Pb/^{204}Pb$, $^{207}Pb/^{204}Pb$, $^{208}Pb/^{204}Pb$ ratios of shoshonites range from 18.42 to 18.75, 15.40–15.70, and 38.45–39.20 (n = 9), the $^{87}Sr/^{86}Sr$ ratios are between 0.70633 and 0.70827 (n = 17), and their $^{143}Nd/^{144}Nd$ values are 0.51223–0.51255 (n = 13) and εNd −1.72 to −7.96. These isotopic compositions overlap or are close to the values of other mafic centres of the Puna (Fig. 13).

The Pb isotopic ratios are enriched relative to the NHRL (Northern Hemisphere Reference Line), pointing out a crustal component's contribution. However, they do not vary with silica or other element concentrations (e.g., Sr, Nd), which is interpreted as mixing end-members having the same isotopic signature for Pb. Several studies have outlined domains within the central Andean orocline (13–28°S) based on radiogenic Pb (Aitcheson et al., 1995; Mamani et al, 2008, 2010; Wörner et al., 2018). These domains would correspond to terranes that were amalgamated to the western Gondwana margin (Ramos, 2008). The Pb isotope ratios of shoshonitic rocks are slightly lower than those of the southern's Puna mafic volcanic rocks (Fig. 13a), suggesting another terrane's involvement. We speculate that Pb ratios of shoshonites reflect the Pampia terrane, whereas the values of mafic volcanoes from the southern Puna are closer to those of the Antofalla domain/-terrane (Mamani et al., 2010) (inset b in Fig. 1).

The shoshonitic sample set shows narrower ranges for Sr and Nd

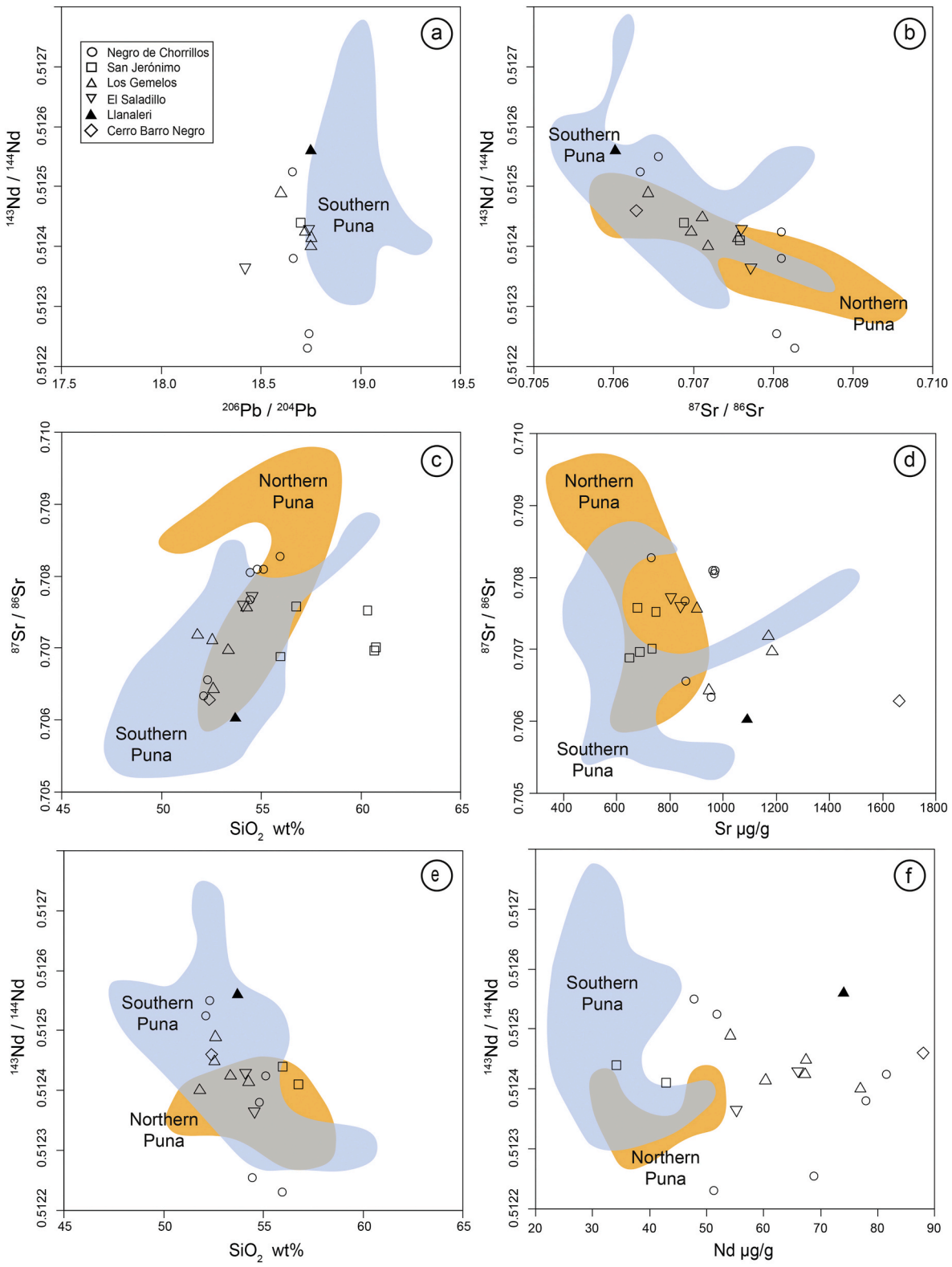

Fig. 13. Sr-Nd-Pb diagrams for shoshonitic volcanic centres of the Puna (data from (Déruelle, 1991; Guzmán et al., 2006; Kay et al., 1994; Krallmann, 1994; Maro et al., 2017; Murray et al., 2015). The compositional fields of the Neogene mafic volcanic rocks of northern Puna (Kay et al., 2010; Krallmann, 1994; Maro et al., 2016b) and southern Puna (Drew et al., 2009; Risse et al., 2013) are also indicated as reference.

isotope ratios compared to northern and southern Puna mafic volcanoes, although they mostly overlap with these distributions (Fig. 13b–f). The general positive trend of $^{87}Sr/^{86}Sr$ isotope ratio against silica of all Puna mafic rocks compiled reveals a typical behaviour of the assimilation and fractional crystallization (AFC) process (DePaolo, 1981) (Fig. 13c), which increases the $^{87}Sr/^{86}Sr$ ratio values by crustal assimilation of older material with higher $^{87}Sr/^{86}Sr$ compositions during differentiation (González-Maurel et al., 2019). The general variation of $^{87}Sr/^{86}Sr$ vs. Sr

(Fig. 13d) is also compatible with the AFC process (González-Maurel et al., 2019; Hildreth and Moorbath, 1988). On the other hand, the assimilation during turbulent ascent (ATA) process (Huppert et al., 1985) has been proposed to explain the evolution of these mafic magmas (Guzmán et al., 2006; Maro et al., 2016b). In this process, the least-evolved magmas may be the most contaminated, and it is documented by reverse trends in SiO_2 and Sr vs. $^{87}Sr/^{86}Sr$ diagrams (González-Maurel et al., 2019). These trends are not dominantly depicted in Fig. 13c–d.

Crustal contamination by magma mixing in San Jerónimo and Negro de Chorrillos shoshonitic magmas is corroborated by physico-chemical disequilibria in crystals and glass. Accordingly, both volcanic centres must be modelled as an open system in which external melts were introduced in the shoshonitic magma. A wide variety of microscopic disequilibrium textures provides unequivocal evidence of the interaction between melts and the magmatic system's inability to reach equilibrium conditions (Streck, 2008). Thus, we find a mismatch of mineral assemblages (e.g., the co-occurrence of olivine and quartz), crystal textures (e.g., dusty or resorbed textured macrocrysts, replacement reactions), and a wide range of compositional variation in the glass. This last feature suggests the contamination by trachytic-trachydacitic melts.

These interactions with pre-existing trachyte-trachydacite crustal melts were relatively limited, e.g., little to no inherited minerals (quartz, feldspars) and a slight change in bulk rock geochemistry. This type of magmatic evolution is typically ascribed to polybaric differentiation within a trans crystal column of magmatic mush (Cashman et al., 2017; Cashman and Edmonds, 2019), and the magmas must be removed from the AFC site and erupted immediately to preserve correlations between indices of differentiation and isotopic ratios (Davidson and de Silva, 1995). According to recent numerical simulations, these mixing processes are produced in a short time, in the order of hours or days (Montagna et al., 2015; Morgavi et al., 2019; Perugini et al., 2010). The wide range obtained for pressure (up to 7.1 kbar, up to ~21.3 km) and the narrow range of temperature (1180–1100 °C) also supports a fast ascent rate (Fig. 9b).

These considerations are common to the origin of shoshonitic and high-K calc-alkaline magmas in the Puna, and they do not resolve how to obtain a shoshonitic magma in specific and rare locations. We suggest that an additional geodynamic factor could be involved. The shoshonitic centres are approximately located in the intersection of the N–S suture between the terranes of Antofalla and Pampia with the major NW-SE fault systems of Lípez-Coranzulí (Cerro Barro Negro volcano) and Calama-Olacapato-El Toro (San Jerónimo, Negro de Chorrillos, El Saladillo and Los Gemelos volcanoes) (Fig, 1). The Antofalla-Pampia suture is a significant weakness zone developed in Paleozoic times along the southwestern margin of Gondwana (Augustsson et al., 2015; Beck and Zandt, 2002; Heredia et al., 2018; Omarini et al., 1999; Ortiz et al., 2019; Ramos, 2010, 2018). Although its precise location on its entire length is still a matter of debate, this suture is essentially sub-parallel to the modern Andean chain in the central Andes. This hypothesis would represent a mechanism by which a preferential terrane boundary distribution could develop a small volume of potassic melts (precursors of the shoshonitic rocks), while the major NW-SE fault systems would favour their ascent to the surface.

Finally, potassic and ultrapotassic (i.e., phlogopite-bearing) magmas in the same eruption are interpreted as pulses of the same magma feeding the volcano. Petrographic and chemical differences are possibly due to changes in the interaction time with the felsic magma. A longer interaction during mixing, within the eruptive time window of hours or days, allowed a practically fully crystallized groundmass in the ultrapotassic rocks, reducing the quantity of glass and forming phlogopite.

6. Conclusions

San Jerónimo and Negro de Chorrillos shoshonitic volcanoes are small monogenetic edifices mainly built by effusive activity, resulting from a Strombolian-type eruption with a Volcanic Explosivity Index (VEI) of 2 (Newhall and Self, 1982). Unspiked K–Ar ages (groundmass) yield 144 ± 3 ka for San Jerónimo and 51 ± 2 ka for Negro de Chorrillos eruptions.

Volcanic products of potassic and ultrapotassic (i.e., phlogopite-bearing) compositions occur in both eruptions. The main petrographic differences are the occurrence of phlogopite and the low glass content in the ultrapotassic rocks. Geochemically, the lava flows of SJ and NdC exhibit the same spinel lherzolite mantle source composition, which is stable in the range of 20–50 km depth for temperatures of 1100–1200 °C. According to the crustal thickness of this part of the Puna, our magmas would be generated at the highest depth of lherzolite's stability field with spinel (40–50 km). The phlogopite would form on its ascent and up to a depth of about 20 km.

Once in the crust, the K-rich magma interacted with a trachytic-trachydacitic melt, on the order of hours or days, producing minor contamination of the mafic magma. This mixing is evidenced petrographically and geochemically, e.g., mismatch of mineral assemblages (co-occurrence of olivine and quartz), disequilibrium crystal textures (dusty zones in plagioclase, embayments in feldspars), and a wide range of compositional variation in the glasses. The presence of potassic and ultrapotassic rocks in the same eruption is interpreted as pulses of the same magma but with differences in interaction time during magma mixing. A longer interaction allowed a practically fully crystallized groundmass in the ultrapotassic rocks.

The scarcity and location of shoshonitic centres, compared with other mafic volcanic centres of the northern and southern Puna, suggest that a preferential N–S terrane boundary distribution could develop a small volume of potassic melts (precursors of the shoshonitic rocks), while the major NW-SE fault systems would favour their ascent to the surface. The eruptive histories of SJ and NdC may give insights on the past and future behaviour of similar volcanoes in other back-arc regions of large plateaus as the Altiplano in the CVZ or the Tibetan plateau.

CRediT author statement

J.L. Fernandez-Turiel: Conceptualization, Investigation, Writing – review & editing, Investigation, data curation. J. Saavedra: Conceptualization, Methodology, Investigation, Writing – original draft preparation. F.J. Perez-Torrado: Conceptualization, Methodology, Investigation. A. Rodriguez-Gonzalez: Conceptualization, Investigation, Visualization. M. Rejas: Resources (geochemical analyses). H. Guillou: Resources (geochronological analysis). M. Aulinas: Investigation, formal analysis.

Declaration of competing interest

The authors declare that they have no known competing financial interests or personal relationships that could have appeared to influence the work reported in this paper.

Acknowledgements

Financial support was provided by Project QUECA (MINECO, ref. CGL 2011-23307). This study was carried out in the Research Consolidated Groups GEOVOL (Canary Islands Government, ULPGC) and GEOPAM (Generalitat de Catalunya, 2017 SGR 1494). We acknowledge the assistance in the analytical work of labGEOTOP Geochemistry Laboratory (infrastructure co-funded by ERDF–EU Ref. CSIC08–4E–001) of GEO3BCN, CSIC, and EPMA Laboratories of CCiTUB (X. Llovet), and D. Fernández, her support on reference management. We thank the collaboration of P. E. Urquizo Furlán. We are grateful to the editor P. Samaniego for the effective handling of the manuscript and P. Grosse and S. Guzmán for providing insightful comments on a preliminary version of this manuscript.

References

Acocella, V., 2014. Structural control on magmatism along divergent and convergent plate boundaries: overview, model, problems. Earth Sci. Rev. 136, 226–288. https://doi.org/10.1016/j.earscirev.2014.05.006.

Acocella, V., Gioncada, A., Omarini, R., Riller, U., Mazzuoli, R., Vezzoli, L., 2011. Tectonomagmatic characteristics of the back-arc portion of the calama–olacapato–el Toro fault zone, central andes. Tectonics 30. https://doi.org/10.1029/2010TC002854.

Aitcheson, S.J., Harmon, R.S., Moorbath, S., Schneider, A., Soler, P., Soria-Escalante, E., Steele, G., Swainbank, I., Wörner, G., 1995. Pb isotopes define basement domains of the Altiplano, central Andes. Geology 23, 555–558. https://doi.org/10.1130/0091-7613(1995)023<0555:PIDBDO>2.3.CO;2.

Allmendinger, R.W., Jordan, T.E., Kay, S.M., Isacks, B.L., 1997. The evolution of the Altiplano-Puna plateau of the central Andes. Annu. Rev. Earth Planet Sci. 25, 139–174. https://doi.org/10.1146/annurev.earth.25.1.139.

Aquater, 1980. Exploración geotérmica del área del cerro Tuzgle, Provincia de Jujuy, República Argentina. Secretaría de Estado de Minería.

Aquater, 1979. Estudio del potential geotérmico de la Provincia de Jujuy, República Argentina. Secretaría de Estado de Minería, Buenos Aires.

Arai, S., 1994. Compositional variation of olivine-chromian spinel in Mg-rich magmas as a guide to their residual spinel peridotites. J. Volcanol. Geoth. Res. 59, 279–293. https://doi.org/10.1016/0377-0273(94)90083-3.

Augustsson, C., Rüsing, T., Niemeyer, H., Kooijman, E., Berndt, J., Bahlburg, H., Zimmermann, U., 2015. 0.3 byr of drainage stability along the Palaeozoic palaeo-Pacific Gondwana margin; a detrital zircon study. J. Geol. Soc. London. https://doi.org/10.1144/jgs2014-065, 2014–065.

Aulinas, M., Garcia-Valles, M., Fernandez-Turiel, J.L., Gimeno, D., Saavedra, J., Gisbert, G., 2015. Insights into the formation of rock varnish in prevailing dusty regions. Earth Surf. Process. Landforms 40, 447–458. https://doi.org/10.1002/esp.3644.

Báez, W., Carrasco Nuñez, G., Giordano, G., Viramonte, J.G., Chiodi, A., 2017. Polycyclic scoria cones of the Antofagasta de la Sierra basin, Southern Puna plateau, Argentina. In: Németh, K., Carrasco-Núñez, G., Aranda-Gómez, J.J., Smith, I.E.M. (Eds.), Monogenetic Volcanism. The Geological Society of London, pp. 311–336. https://doi.org/10.1144/SP446.3.

Baier, J., Audétat, A., Keppler, H., 2008. The origin of the negative niobium tantalum anomaly in subduction zone magmas. Earth Planet Sci. Lett. 267, 290–300. https://doi.org/10.1016/j.epsl.2007.11.032.

Barnes, J.B., Ehlers, T.A., 2009. End member models for Andean Plateau uplift. Earth Sci. Rev. 97, 105–132. https://doi.org/10.1016/j.earscirev.2009.08.003.

Barnes, S.J., Roeder, P.L., 2001. The range of spinel compositions in terrestrial mafic and ultramafic rocks. J. Petrol. 42, 2279–2302. https://doi.org/10.1093/petrology/42.12.2279.

Beck, S.L., Zandt, G., 2002. The nature of orogenic crust in the central Andes. J. Geophys. Res. Solid Earth 107. https://doi.org/10.1029/2000JB000124. ESE 7-1.

Beck, S.L., Zandt, G., Ward, K.M., Scire, A., 2015. Multiple styles and scales of lithospheric foundering beneath the Puna Plateau, central Andes. In: DeCelles, P.G., Ducea, M.N., Carrapa, B., Kapp, P.A. (Eds.), Geodynamics of a Cordilleran Orogenic System: the Central Andes of Argentina and Northern Chile. Geological Society of America, pp. 43–60. https://doi.org/10.1130/2015.1212(03.

Bédard, J.H., 2005. Partitioning coefficients between olivine and silicate melts. Lithos 83, 394–419. https://doi.org/10.1016/j.lithos.2005.03.011.

Beermann, O., Holtz, F., Duesterhoeft, E., 2017. Magma storage conditions and differentiation of the mafic Lower Pollara volcanics, Salina Island, Aeolian Islands, Italy: implications for the formation conditions of shoshonites and potassic rocks. Contrib. Mineral. Petrol. 172, 37. https://doi.org/10.1007/s00410-017-1363-z.

Bianchi, M., Heit, B., Jakovlev, A., Yuan, X., Kay, S.M., Sandvol, E., Alonso, R.N., Coira, B., Brown, L., Kind, R., Comte, D., 2013. Teleseismic tomography of the southern Puna plateau in Argentina and adjacent regions. Tectonophysics 586, 65–83. https://doi.org/10.1016/j.tecto.2012.11.016.

Bonali, F.L., Corazzato, C., Tibaldi, A., 2012. Elastic stress interaction between faulting and volcanism in the Olacapato–San Antonio de Los Cobres area (Puna plateau, Argentina). Global Planet. Change 90–91, 104–120. https://doi.org/10.1016/j.gloplacha.2011.08.002.

Boynton, W.V., 1984. Chapter 3 - cosmochemistry of the rare Earth elements: meteorite studies. In: Henderson, P. (Ed.), Developments in Geochemistry. Elsevier, pp. 63–114. https://doi.org/10.1016/B978-0-444-42148-7.50008-3.

Calixto, F.J., Sandvol, E., Kay, S., Mulcahy, P., Heit, B., Yuan, X., Coira, B., Comte, D., Alvarado, P., 2013. Velocity structure beneath the southern Puna plateau: evidence for delamination. Geochem. Geophys. Geosyst. 14, 4292–4305. https://doi.org/10.1002/ggge.20266.

Campbell, I.H., Stepanov, A.S., Liang, H.-Y., Allen, C.M., Norman, M.D., Zhang, Y.-Q., Xie, Y.-W., 2014. The origin of shoshonites: new insights from the Tertiary high-potassium intrusions of eastern Tibet. Contrib. Mineral. Petrol. 167, 983. https://doi.org/10.1007/s00410-014-0983-9.

Carlier, G., Lorand, J., Liegeois, J., Fornari, M., 2005. Potassic-ultrapotassic mafic rocks delineate two-lithospheric mantle blocks beneath the southern Peruvian Altiplano. Geology 33, 601–604. https://doi.org/10.1130/G21643.1.

Cashman, K.V., Edmonds, M., 2019. Mafic glass compositions: a record of magma storage conditions, mixing and ascent. Philos. Trans. Royal Soc. A 377, 20180004. https://doi.org/10.1098/rsta.2018.0004.

Cashman, K.V., Sparks, R.S.J., Blundy, J.D., 2017. Vertically extensive and unstable magmatic systems: a unified view of igneous processes. Science 355. https://doi.org/10.1126/science.aag3055 eaag3055.

Chapman, A.D., Ducea, M.N., McQuarrie, N., Coble, M., Petrescu, L., Hoffman, D., 2015. Constraints on plateau architecture and assembly from deep crustal xenoliths, northern Altiplano (SE Peru). Geol. Soc. Am. Bull. 127, 1777–1797. https://doi.org/10.1130/B31206.1.

Charbit, S., Guillou, H., Turpin, L., 1998. Cross calibration of K–Ar standard minerals using an unspiked Ar measurement technique. Chem. Geol. 150, 147–159. https://doi.org/10.1016/S0009-2541(98)00049-7.

Coira, B., Kay, S.M., 1993. Implications of quaternary volcanism at cerro Tuzgle for crustal and mantle evolution of the Puna plateau, central andes, Argentina. Contrib. Mineral. Petrol. 113, 40–58. https://doi.org/10.1007/BF00320830.

Coira, B., Kay, S.M., Viramonte, J., 1993. Upper Cenozoic magmatic evolution of the Argentine Puna—a model for changing subduction geometry. Int. Geol. Rev. 35, 677–720. https://doi.org/10.1080/00206819309465552.

Coira, B.L., Paris, G., 1981. Estratigrafía volcánica del área del Cerro Tuzgle (23° 50' 24° 25' Latitud S y 66° 15' 66° 45' Longitude O), Provincials de Jujuy-Salta. In: Actas. Presented at the VIII Congreso Geológico Argentino, San Luis, pp. 659–671.

Condamine, P., Médard, E., 2014. Experimental melting of phlogopite-bearing mantle at 1 GPa: implications for potassic magmatism. Earth Planet Sci. Lett. 397, 80–92. https://doi.org/10.1016/j.epsl.2014.04.027.

Davidson, J.P., de Silva, S.L., 1995. Late cenozoic magmatism of the Bolivian Altiplano. Contrib. Mineral. Petrol. 119, 387–408. https://doi.org/10.1007/BF00286937.

Davidson, J.P., Morgan, D.J., Charlier, B.L.A., Harlou, R., Hora, J.M., 2007a. Microsampling and isotopic analysis of igneous rocks: implications for the study of magmatic systems. Annu. Rev. Earth Planet Sci. 35, 273–311. https://doi.org/10.1146/annurev.earth.35.031306.140211.

Davidson, J.P., Turner, S., Handley, H., Macpherson, C., Dosseto, A., 2007b. Amphibole "sponge" in arc crust? Geology 35, 787–790. https://doi.org/10.1130/G23637A.1.

de Silva, S.L., Kay, S.M., 2018. Turning up the heat: high-flux magmatism in the central andes. Elements 14, 245–250. https://doi.org/10.2138/gselements.14.4.245.

Deer, W.A., Frs, Howie R.A., Zussman, J., 2013. An Introduction to the Rock-Forming Minerals. Mineralogical Society of Great Britain and Ireland. https://doi.org/10.1180/DHZ.

Delph, J.R., Ward, K.M., Zandt, G., Ducea, M.N., Beck, S.L., 2017. Imaging a magma plumbing system from MASH zone to magma reservoir. Earth Planet Sci. Lett. 457, 313–324. https://doi.org/10.1016/j.epsl.2016.10.008.

DePaolo, D.J., 1981. Trace element and isotopic effects of combined wallrock assimilation and fractional crystallization. Earth Planet Sci. Lett. 53, 189–202. https://doi.org/10.1016/0012-821X(81)90153-9.

Déruelle, B., 1991. Petrology of Quaternary shoshonitic lavas of northwestern Argentina. In: Harmon, R.S., Rapela, C.W. (Eds.), Andean Magmatism and its Tectonic Setting. Geological Society of America, pp. 201–216. https://doi.org/10.1130/SPE265-p201.

Déruelle, B., 1982. Petrology of the plio-quaternary volcanism of the south-central and meridional andes. J. Volcanol. Geoth. Res. 14, 77–124. https://doi.org/10.1016/0377-0273(82)90044-0.

Di Traglia, F., Morelli, S., Casagli, N., Garduño Monroy, V.H., 2014. Semi-automatic delimitation of volcanic edifice boundaries: validation and application to the cinder cones of the tancitaro–nueva italia region (Michoacán–Guanajuato volcanic field, Mexico). Geomorphology 219, 152–160. https://doi.org/10.1016/j.geomorph.2014.05.002.

Drew, S.T., Ducea, M.N., Schoenbohm, L.M., 2009. Mafic volcanism on the Puna Plateau, NW Argentina: implications for lithospheric composition and evolution with an emphasis on lithospheric foundering. Lithosphere 1, 305–318. https://doi.org/10.1130/L54.1.

Ducea, M.N., Seclaman, A.C., Murray, K.E., Jianu, D., Schoenbohm, L.M., 2013. Mantle-drip magmatism beneath the Altiplano-Puna plateau, central Andes. Geology 41, 915–918. https://doi.org/10.1130/G34509.1.

Fernandez-Turiel, J.L., Perez–Torrado, F.J., Rodriguez-Gonzalez, A., Saavedra, J., Carracedo, J.C., Rejas, M., Lobo, A., Osterrieth, M., Carrizo, J.I., Esteban, G., Gallardo, J., Ratto, N., 2019. The large eruption 4.2 ka cal BP in Cerro Blanco, Central Volcanic Zone, Andes: insights to the Holocene eruptive deposits in the southern Puna and adjacent regions. Estud. Geol. 75 (1), e088. https://doi.org/10.3989/egeol.43438.515.

Fernandez-Turiel, J.L., Perez-Torrado, F.J., Saavedra, J., Rejas, M., Rodriguez-Gonzalez, A., Aulinas, M., 2020. Dataset of whole-rock, glass and mineral geochemical data of recent shoshonitic volcanism of Puna, Central Volcanic Zone of Andes: San Jerónimo and Negro de Chorrillos volcanoes. Reposit. Digital.CSIC. https://doi.org/10.20350/digitalCSIC/10527.

Filipovich, R., Báez, W., Groppelli, G., Ahumada, F., Aldega, L., Becchio, R., Berardi, G., Bigi, S., Caricchi, C., Chiodi, A., Corrado, S., Astis, G.D., Benedetti, A.A., Invernizzi, C., Norini, G., Soligo, M., Taviani, S., Viramonte, J., Giordano, G., 2020. Geological map of the tocomar basin (Puna plateau, NW Argentina). Implication for the geothermal system investigation. Energies 13, 5492.

Foley, S., 1992. Vein-plus-wall-rock melting mechanisms in the lithosphere and the origin of potassic alkaline magmas. Lithos 28, 435–453. https://doi.org/10.1016/0024-4937(92)90018-T.

Foley, S.F., Venturelli, G., Green, D.H., Toscani, L., 1987. The ultrapotassic rocks: characteristics, classification, and constraints for petrogenetic models. Earth Sci. Rev. 24, 81–134. https://doi.org/10.1016/0012-8252(87)90001-8.

Fornaciai, A., Favalli, M., Karátson, D., Tarquini, S., Boschi, E., 2012. Morphometry of scoria cones, and their relation to geodynamic setting: a DEM-based analysis. J. Volcanol. Geoth. Res. 217–218, 56–72. https://doi.org/10.1016/j.jvolgeores.2011.12.012.

Förster, M., Buhre, S., Xu, B., Prelević, D., Mertz-Kraus, R., Foley, S., 2019. Two-stage origin of K-enrichment in ultrapotassic magmatism simulated by melting of experimentally metasomatized mantle. Minerals 10, 41.

Franceschinis, P.R., Rapalini, A.E., Escayola, M.P., Luppo, T., 2016. Paleomagnetic studies on the late ediacaran – early cambrian puncoviscana and the late cambrian campanario formations, NW Argentina: new paleogeographic constraints for the Pampia terrane. J South Am. Earth Sci. 70, 145–161. https://doi.org/10.1016/j.jsames.2016.04.007.

Fritschle, T., Prelević, D., Foley, S.F., Jacob, D.E., 2013. Petrological characterization of the mantle source of Mediterranean lamproites: indications from major and trace elements of phlogopite. Chem. Geol. 353, 267–279. https://doi.org/10.1016/j.chemgeo.2012.09.006.

Fuhrman, M.L., Lindsley, D.H., 1988. Ternary-feldspar modeling and thermometry. Am. Mineral. 73, 201–215.

Garzione, C.N., McQuarrie, N., Perez, N.D., Ehlers, T.A., Beck, S.L., Kar, N., Eichelberger, N., Chapman, A.D., Ward, K.M., Ducea, M.N., Lease, R.O., Poulsen, C. J., Wagner, L.S., Saylor, J.E., Zandt, G., Horton, B.K., 2017. Tectonic evolution of the Central Andean Plateau and implications for the growth of plateaus. Annu. Rev. Earth Planet Sci. 45, 529–559. https://doi.org/10.1146/annurev-earth-063016-020612.

Gibson, S.A., Thompson, R.N., Leonardos, O.H., Dickin, A.P., Mitchell, J.G., 1995. The late cretaceous impact of the trindade mantle plume: evidence from large-volume, mafic, potassic magmatism in SE Brazil. J. Petrol. 36, 189–229. https://doi.org/10.1093/petrology/36.1.189.

Gill, R., 2010. Igneous Rocks and Processes: A Practical Guide. Wiley-Blackwell.

Gill, R.C.O., Aparicio, A., El Azzouzi, M., Hernandez, J., Thirlwall, M.F., Bourgois, J., Marriner, G.F., 2004. Depleted arc volcanism in the Alboran Sea and shoshonitic volcanism in Morocco: geochemical and isotopic constraints on Neogene tectonic processes. Lithos 78, 363–388. https://doi.org/10.1016/j.lithos.2004.07.002.

González-Maurel, O., Godoy, B., le Roux, P., Rodríguez, I., Marín, C., Menzies, A., Bertin, D., Morata, D., Vargas, M., 2019. Magmatic differentiation at La Poruña scoria cone, Central Andes, northern Chile: evidence for assimilation during turbulent ascent processes, and genetic links with mafic eruptions at adjacent San Pedro volcano. Lithos 338 (339), 128–140. https://doi.org/10.1016/j.lithos.2019.03.033.

Green, T.H., Blundy, J.D., Adam, J., Yaxley, G.M., 2000. SIMS determination of trace element partition coefficients between garnet, clinopyroxene and hydrous basaltic liquids at 2–7.5 GPa and 1080–1200°C. Lithos 53, 165–187. https://doi.org/10.1016/S0024-4937(00)00023-2.

Grosse, P., Guzman, S., Petrinovic, I., 2017. Volcanes compuestos cenozoicos del noroeste argentino. In: Muruaga, C.M., Grosse, P. (Eds.), Ciencias de La Tierra y Recursos Naturales Del NOA, Relatorio Del XX Congreso Geológico Argentino. San Miguel de Tucumán, pp. 484–517.

Grosse, P., Ochi Ramacciotti, M.L., Escalante Fochi, F., Guzmán, S., Orihashi, Y., Sumino, H., 2020. Geomorphology, morphometry, spatial distribution and ages of mafic monogenetic volcanoes of the Peinado and Incahuasi fields, southernmost Central Volcanic Zone of the Andes. J. Volcanol. Geoth. Res. 401, 106966. https://doi.org/10.1016/j.jvolgeores.2020.106966.

Guillou, H., Carracedo, J.C., Torrado, F.P., Badiola, E.R., 1996. K-Ar ages and magnetic stratigraphy of a hotspot-induced, fast grown oceanic island: el Hierro, Canary Islands. J. Volcanol. Geoth. Res. 73, 141–155. https://doi.org/10.1016/0377-0273(96)00021-2.

Guzmán, S., Grosse, P., Montero-López, C., Hongn, F., Pilger, R., Petrinovic, I., Seggiaro, R., Aramayo, A., 2014. Spatial–temporal distribution of explosive volcanism in the 25–28°S segment of the Andean Central Volcanic Zone. Tectonophysics 636, 170–189. https://doi.org/10.1016/j.tecto.2014.08.013.

Guzmán, S.R., Petrinovic, I.A., Brod, J.A., 2006. Pleistocene mafic volcanoes in the puna–cordillera oriental boundary, NW-Argentina. J. Volcanol. Geoth. Res. 158, 51–69. https://doi.org/10.1016/j.jvolgeores.2006.04.014.

Haag, M.B., Baez, W.A., Sommer, C.A., Arnosio, J.M., Filipovich, R.E., 2019. Geomorphology and spatial distribution of monogenetic volcanoes in the southern Puna Plateau (NW Argentina). Geomorphology 342, 196–209. https://doi.org/10.1016/j.geomorph.2019.06.008.

Harmon, R.S., Barreiro, B.A., Moorbath, S., Hoefs, J., Francis, P.W., Thorpe, R.S., Déruelle, B., McHugh, J., Viglino, J.A., 1984. Regional O-, Sr-, and Pb-isotope relationships in late Cenozoic calc-alkaline lavas of the Andean Cordillera. J. Geol. Soc. London 141, 803. https://doi.org/10.1144/gsjgs.141.5.0803.

Hausen, H., 1937. Zur Kenntnis der magmengesteine der Chilenischen Atacama-Wüste. N. Jb. Min. Geol Pal., Beil. - Bd. 73, 151–238.

Heit, B., Bianchi, M., Yuan, X., Kay, S.M., Sandvol, E., Kumar, P., Kind, R., Alonso, R.N., Brown, L.D., Comte, D., 2014. Structure of the crust and the lithosphere beneath the southern Puna plateau from teleseismic receiver functions. Earth Planet Sci. Lett. 385, 1–11. https://doi.org/10.1016/j.epsl.2013.10.017.

Heredia, N., García-Sansegundo, J., Gallastegui, G., Farias, P., Giacosa, R., Alonso, J.L., Busquets, P., Charrier, R., Clariana, P., Colombo, F., Cuesta, A., Gallastegui, J., Giambiagi, L., González-Menéndez, L., Limarino, C.O., Martín- González, F., Méndez-Bedia, I., Pedreira, D., Quintana, L., Rodríguez-Fernández, L.R., Rubio-Ordóñez, A., Seggiaro, R., Serra-Varela, S., Spalletti, L., Cardó, R., Ramos, V.A., 2018. Evolución geodinámica de los Andes argentino-chilenos y la Península Antártica durante el Neoproterozoico tardío y el Paleozoico. Trab. Geol. 36, 237–278. https://doi.org/10.17811/tdg.36.2016.237-278.

Hibbard, M.J., 1981. The magma mixing origin of mantled feldspars. Contrib. Mineral. Petrol. 76, 158–170. https://doi.org/10.1007/BF00371956.

Hildreth, W., Moorbath, S., 1988. Crustal contributions to arc magmatism in the Andes of Central Chile. Contrib. Mineral. Petrol. 98, 455–489. https://doi.org/10.1007/BF00372365.

Hirschmann, M.M., Ghiorso, M.S., Stolper, M., 1999. Calculation of peridotite partial melting from thermodynamic models of minerals and melts. II. Isobaric variations in melts near the solidus and owing to variable source composition. J. Petrol. 40, 297–313. https://doi.org/10.1093/petroj/40.2.297.

Hoke, L., Lamb, S., 2007. Cenozoic behind-arc volcanism in the Bolivian Andes, South America: implications for mantle melt generation and lithospheric structure. J. Geol. Soc. London 164, 795. https://doi.org/10.1144/0016-76492006-092.

Hörmann, P.K., Pichler, H., Zeil, W., 1973. New data on the young volcanism in the Puna of NW-Argentina. Geol. Rundsch. 62, 397–418. https://doi.org/10.1007/BF01840106.

Huppert, H.E., Stephen, R., Sparks, J., 1985. Cooling and contamination of mafic and ultramafic magmas during ascent through continental crust. Earth Planet Sci. Lett. 74, 371–386. https://doi.org/10.1016/S0012-821X(85)80009-1.

Ibarra, F., Liu, S., Meeßen, C., Prezzi, C.B., Bott, J., Scheck-Wenderoth, M., Sobolev, S., Strecker, M.R., 2019. 3D data-derived lithospheric structure of the Central Andes and its implications for deformation: insights from gravity and geodynamic modelling. Tectonophysics 766, 453–468. https://doi.org/10.1016/j.tecto.2019.06.025.

Irvine, T.N., Baragar, W.R.A., 1971. A guide to the chemical classification of the common volcanic rocks. Can. J. Earth Sci. 8, 523–548. https://doi.org/10.1139/e71-055.

Janoušek, V., Farrow, C.M., Erban, V., 2006. Interpretation of whole-rock geochemical data in igneous geochemistry: introducing geochemical data toolkit (GCDkit). J. Petrol. 47, 1255–1259. https://doi.org/10.1093/petrology/egl013.

Janoušek, V., Moyen, J.-F., Martin, H., Erban, V., Farrow, C., 2016. Geochemical Modelling of Igneous Processes – Principles and Recipes in R Language, Bringing the Power of R to a Geochemical Community, first ed. Springer Geochemistry. Springer-Verlag Berlin Heidelberg.

Jiménez, N., López-Velásquez, S., 2008. Magmatism in the Huarina belt, Bolivia, and its geotectonic implications. Tectonophysics 459, 85–106. https://doi.org/10.1016/j.tecto.2007.10.012.

Kawamoto, T., 1992. Dusty and honeycomb plagioclase: indicators of processes in the Uchino stratified magma chamber, Izu Peninsula, Japan. J. Volcanol. Geoth. Res. 49, 191–208. https://doi.org/10.1016/0377-0273(92)90014-5.

Kay, R.W., Mahlburg Kay, S., 1993. Delamination and delamination magmatism. Tectonophysics 219, 177–189. https://doi.org/10.1016/0040-1951(93)90295-U.

Kay, S.M., Coira, B., Mpodozis, C., 2008. Field trip guide: neogene evolution of the central andean Puna Plateau and southern central volcanic zone. In: Kay, S.M., Ramos, V.A. (Eds.), Field Trip Guides to the Backbone of the Americas in the Southern and Central Andes: Ridge Collision, Shallow Subduction, and Plateau Uplift, Field Guide. Geological Society of America, pp. 117–181. https://doi.org/10.1130/2008.0013(05.

Kay, S.M., Coira, B., Viramonte, J., 1994. Young mafic back arc volcanic rocks as indicators of continental lithospheric delamination beneath the Argentine Puna Plateau, central Andes. J. Geophys. Res. Solid Earth 99, 24323–24339. https://doi.org/10.1029/94JB00896.

Kay, S.M., Coira, B.L., 2009. Shallowing and steepening subduction zones, continental lithospheric loss, magmatism, and crustal flow under the Central Andean Altiplano-Puna Plateau. In: Kay, S.M., Ramos, V.A., Dickinson, W.R. (Eds.), Backbone of the Americas: Shallow Subduction, Plateau Uplift, and Ridge and Terrane Collision, Memoir. Geological Society of America, pp. 229–259. https://doi.org/10.1130/2009.1204(11.

Kay, S.M., Coira, B.L., Caffe, P.J., Chen, C.-H., 2010. Regional chemical diversity, crustal and mantle sources and evolution of central Andean Puna plateau ignimbrites. J. Volcanol. Geoth. Res. 198, 81–111. https://doi.org/10.1016/j.jvolgeores.2010.08.013.

Kay, S.M., Mpodozis, C., Coira, B., 1999. Neogene magmatism, tectonism, and mineral deposits of the Central Andes (22° to 33° S Latitude). In: Skinner, B.J. (Ed.), Geology and Ore Deposits of the Central Andes. Special Publication. Society of Economic Geology, pp. 27–59. https://doi.org/10.5382/SP.07.02.

Kereszturi, G., Jordan, G., Németh, K., Dóniz-Páez, J.F., 2012. Syn-eruptive morphometric variability of monogenetic scoria cones. Bull. Volcanol. 74, 2171–2185. https://doi.org/10.1007/s00445-012-0658-1.

Knox, W., Kay, S.M., Coira, B., 1989. Geochemical evidence on the origin of Quaternary basaltic andesites of the Puna, northwestern Argentina. Rev. Asoc. Geol. Argent. 44, 194–206.

Krallmann, A., 1994. Petrographische und geochemische Untersuchungen an jungen, basischen Vulkaniten im Bereich des Calama-Olacapato-El Toro - lineamentes östlich der Vulkankette, NW - Argentinien. Clausthal. Geowiss. Diss. 45, 1–160.

Lanza, F., Tibaldi, A., Bonali, F.L., Corazzato, C., 2013. Space–time variations of stresses in the miocene–quaternary along the calama–olacapato–el Toro fault zone, central andes. Tectonophysics 593, 33–56. https://doi.org/10.1016/j.tecto.2013.02.029.

Larrea, P., Galé, C., Ubide, T., Widom, E., Lago, M., França, Z., 2014. Magmatic evolution of graciosa (Azores, Portugal). J. Petrol. 55, 2125–2154. https://doi.org/10.1093/petrology/egu052.

LaTourrette, T., Hervig, R.L., Holloway, J.R., 1995. Trace element partitioning between amphibole, phlogopite, and basanite melt. Earth Planet Sci. Lett. 135, 13–30. https://doi.org/10.1016/0012-821X(95)00146-4.

Le Bas, M.J., Le Maitre, R.W., Streckeisen, A., Zanettin, B., IUGS Subcommission on the Systematics of Igneous Rocks, 1986. A chemical classification of volcanic rocks based on the total Alkali-silica diagram. J. Petrol. 27, 745–750. https://doi.org/10.1093/petrology/27.3.745.

Liang, X., Sandvol, E., Kay, S., Heit, B., Yuan, X., Mulcahy, P., Chen, C., Brown, L., Comte, D., Alvarado, P., 2014. Delamination of southern Puna lithosphere revealed by body wave attenuation tomography. J. Geophys. Res. Solid Earth 119, 549–566. https://doi.org/10.1002/2013JB010309.

Libourel, G., 1999. Systematics of calcium partitioning between olivine and silicate melt: implications for melt structure and calcium content of magmatic olivines. Contrib. Mineral. Petrol. 136, 63–80. https://doi.org/10.1007/s004100050524.

Linares, E., Gonzalez, R.R., 1990. Catálogo de edades radimétricas de la República Argentina, años 1957-1987, Publicaciones especiales de la Asociación Geológica Argentina. Serie "B", Didáctica y complementaria. Asociación Geológica Argentina, Buenos Aires.

Liu, C.-Z., Wu, F.-Y., Chung, S.-L., Zhao, Z.-D., 2011. Fragments of hot and metasomatized mantle lithosphere in Middle Miocene ultrapotassic lavas, southern Tibet. Geology 39, 923–926. https://doi.org/10.1130/G32172.1.

Maaløe, S., Aoki, K., 1977. The major element composition of the upper mantle estimated from the composition of lherzolites. Contrib. Mineral. Petrol. 63, 161–173. https://doi.org/10.1007/BF00398777.

Mamani, M., Tassara, A., Wörner, G., 2008. Composition and structural control of crustal domains in the central Andes. Geochem. Geophys. Geosyst. 9 https://doi.org/10.1029/2007GC001925.

Mamani, M., Wörner, G., Sempere, T., 2010. Geochemical variations in igneous rocks of the Central Andean orocline (13°S to 18°S): tracing crustal thickening and magma generation through time and space. Geol. Soc. Am. Bull. 122, 162–182. https://doi.org/10.1130/B26538.1.

Mangan, M.T., Cashman, K.V., 1996. The structure of basaltic scoria and reticulite and inferences for vesiculation, foam formation, and fragmentation in lava fountains. J. Volcanol. Geoth. Res. 73, 1–18. https://doi.org/10.1016/0377-0273(96)00018-2.

Maro, G., Caffe, P.J., 2016. Neogene monogenetic volcanism from the Northern Puna region: products and eruptive styles. Geol. Soc. Lond. Spec. Publ. 446, 337. https://doi.org/10.1144/SP446.6.

Maro, G., Caffe, P.J., 2013. Primer registro de lavas shoshoníticas en Puna norte, el cerro Barro Negro. In: Actas. Presented at the 2do Simposio sobre Petrología Ígnea y Metalogénesis Asociada, San Luis, p. 51.

Maro, G., Caffe, P.J., Baez, W., 2017. Volcanismo monogenético máfico cenozoico de la Puna. In: Muruaga, C.M., Grosse, P. (Eds.), Ciencias de La Tierra y Recursos Naturales Del NOA, Relatorio Del XX Congreso Geológico Argentino. San Miguel de Tucumán, pp. 548–557, 2222.

Maro, G., Caffe, P.J., Jofré, C., 2016a. Xenolitos ultramáficos en lavas máficas neógenas de la Puna Norte. Rev. Asoc. Geol. Argent. 73, 280–291.

Maro, G., Caffe, P.J., Romer, R.L., Trumbull, R.B., 2016b. Neogene mafic magmatism in the Northern Puna Plateau, Argentina: generation and evolution of a back-arc volcanic suite. J. Petrol. 58, 1591–1617. https://doi.org/10.1093/petrology/egx066, 3333.

McGlashan, N., Brown, L., Kay, S., 2008. Crustal thickness in the central Andes from teleseismically recorded depth phase precursors. Geophys. J. Int. 175, 1013–1022. https://doi.org/10.1111/j.1365-246X.2008.03897.x.

McLeod, C.L., Davidson, J.P., Nowell, G.M., de Silva, S.L., Schmitt, A.K., 2013. Characterizing the continental basement of the Central Andes: constraints from Bolivian crustal xenoliths. Geol. Soc. Am. Bull. 125, 985–997. https://doi.org/10.1130/B30721.1.

Meixner, A., Sarchi, C., Lucassen, F., Becchio, R., Caffe, P.J., Lindsay, J., Rosner, M., Kasemann, S.A., 2020. Lithium concentrations and isotope signatures of Palaeozoic basement rocks and Cenozoic volcanic rocks from the Central Andean arc and back-arc. Miner. Deposits 55, 1071–1084. https://doi.org/10.1007/s00126-019-00915-2.

Michelfelder, G.S., Feeley, T.C., Wilder, A.D., Klemetti, E.W., 2013. Modification of the continental crust by subduction zone magmatism and vice-versa: across-strike geochemical variations of silicic lavas from individual eruptive centers in the Andean Central Volcanic Zone. Geosciences 3, 633–667. https://doi.org/10.3390/geosciences3040633.

Montagna, C.P., Papale, P., Longo, A., 2015. Timescales of mingling in shallow magmatic reservoirs. Geol. Soc. Lond. Spec. Publ. 422, 131. https://doi.org/10.1144/SP422.6.

Morgavi, D., Arienzo, I., Montagna, C., Perugini, D., Dingwell, D.B., 2019. Magma mixing: history and dynamics of an eruption trigger. In: Gottsmann, J., Neuberg, J., Scheu, B. (Eds.), Volcanic Unrest : from Science to Society. Springer International Publishing, Cham, pp. 123–137. https://doi.org/10.1007/11157_2017_30.

Morgavi, D., Arzilli, F., Pritchard, C., Perugini, D., Mancini, L., Larson, P., Dingwell, D.B., 2016. The Grizzly Lake complex (Yellowstone Volcano, USA): mixing between basalt and rhyolite unraveled by microanalysis and X-ray microtomography. Lithos 260, 457–474. https://doi.org/10.1016/j.lithos.2016.03.026.

Morimoto, N., 1988. Nomenclature of pyroxenes. Mineral. Petrol. 39, 55–76. https://doi.org/10.1007/BF01226262.

Mulcahy, P., Chen, C., Kay, S.M., Brown, L.D., Isacks, B.L., Sandvol, E., Heit, B., Yuan, X., Coira, B.L., 2014. Central Andean mantle and crustal seismicity beneath the Southern Puna plateau and the northern margin of the Chilean-Pampean flat slab. Tectonics 33, 1636–1658. https://doi.org/10.1002/2013TC003393.

Murray, K.E., Ducea, M.N., Schoenbohm, L., 2015. Foundering-driven lithospheric melting: the source of central Andean mafic lavas on the Puna Plateau (22°S–27°S). In: DeCelles, P.G., Ducea, M.N., Carrapa, B., Kapp, P.A. (Eds.), Geodynamics of a Cordilleran Orogenic System: the Central Andes of Argentina and Northern Chile, Memoir. Geological Society of America, pp. 139–166. https://doi.org/10.1130/2015.1212(08.

Naranjo, J.A., Villa, V., Ramírez, C., Pérez de Arce, C., 2018. Volcanism and tectonism in the southern Central Andes: tempo, styles, and relationships. Geosphere 14, 626–641. https://doi.org/10.1130/GES01350.1.

Newhall, C.G., Self, S., 1982. The volcanic explosivity index (VEI) an estimate of explosive magnitude for historical volcanism. J. Geophys. Res.: Oceans 87, 1231–1238. https://doi.org/10.1029/JC087iC02p01231.

Norini, G., Baez, W., Becchio, R., Viramonte, J., Giordano, G., Arnosio, M., Pinton, A., Groppelli, G., 2013. The calama–olacapato–el Toro fault system in the Puna plateau, central andes: geodynamic implications and stratovolcanoes emplacement. Tectonophysics 608, 1280–1297. https://doi.org/10.1016/j.tecto.2013.06.013.

Norini, G., Cogliati, S., Baez, W., Arnosio, M., Bustos, E., Viramonte, J., Groppelli, G., 2014. The geological and structural evolution of the Cerro Tuzgle Quaternary stratovolcano in the back-arc region of the Central Andes, Argentina. J. Volcanol. Geoth. Res. 285, 214–228. https://doi.org/10.1016/j.jvolgeores.2014.08.023.

Omarini, R.H., Sureda, R.J., Götze, H.-J., Seilacher, A., Pflüger, F., 1999. Puncoviscana folded belt in northwestern Argentina: testimony of Late Proterozoic Rodinia fragmentation and pre-Gondwana collisional episodes. Int. J. Earth Sci. 88, 76–97. https://doi.org/10.1007/s005310050247.

Ortiz, A., Quiroga, M., Becchio, R., Hauser, N., Monteros, E., 2019. The lower paleozoic plutonic-volcanic connection in the eastern magmatic belt, SW Gondwana, northern Puna Argentina. J. South Am. Earth Sci. 95, 102306. https://doi.org/10.1016/j.jsames.2019.102306.

Peccerillo, A., Taylor, S.R., 1976. Geochemistry of Eocene calc-alkaline volcanic rocks from the Kastamonu area, Northern Turkey. Contrib. Mineral. Petrol. 58, 63–81. https://doi.org/10.1007/BF00384745.

Perugini, D., Poli, G., Petrelli, M., De Campos, C.P., Dingwell, D.B., 2010. Time-scales of recent Phlegrean Fields eruptions inferred from the application of a 'diffusive fractionation' model of trace elements. Bull. Volcanol. 72, 431–447. https://doi.org/10.1007/s00445-009-0329-z.

Petrinovic, I., Arnosio, J.M., Alvarado, G.E., Guzmán, S., 2005. Erupciones freáticas sintectónicas en el campo geotérmico de Tocomar. Salta. Rev. Asoc. Geol. Argent. 60, 132–141.

Petrinovic, I.A., 2008. Los Volcanes Gemelos de La Poma, El Saladillo, Negro de Chorrillos y San Jerónimo, las erupciones más recientes en el borde oriental de la Puna. In: Sitios de Interés Geológico de La República Argentina, Anales. Servicio Geológico Minero Argentino (SEGEMAR), Buenos Aires, pp. 37–45.

Petrinovic, I.A., Colombo Piñol, F., 2006. Phreatomagmatic and phreatic eruptions in locally extensive settings of southern central andes: the tocomar volcanic centre (24°10′s–66°34′W), Argentina. J. Volcanol. Geoth. Res. 158, 37–50. https://doi.org/10.1016/j.jvolgeores.2006.04.013.

Petrinovic, I.A., Grosse, P., Guzman, S., Caffe, P.J., 2017. Evolución del volcanismo cenozoico en la Puna Argentina. In: Muruaga, C.M., Grosse, P. (Eds.), Ciencias de La Tierra y Recursos Naturales Del NOA, Relatorio Del XX Congreso Geológico Argentino. San Miguel de Tucumán, pp. 469–483.

Putirka, K.D., 2008. Thermometers and barometers for volcanic systems. Rev. Mineral. Geochem. 69, 61–120. https://doi.org/10.2138/rmg.2008.69.3.

Ramos, V.A., 2018. The famatinian orogen along the protomargin of western Gondwana: evidence for a nearly continuous ordovician magmatic arc between Venezuela and Argentina. In: Folguera, A., Contreras-Reyes, E., Heredia, N., Encinas, A., B Iannelli, S., Oliveros, V., Dávila, F.M., Collo, G., Giambiagi, L., Maksymowicz, A., Iglesia Llanos, M.P., Turienzo, M., Naipauer, M., Orts, D., Litvak, V., Alvarez, O., Arriagada, C. (Eds.), The Evolution of the Chilean-Argentinean Andes. Springer International Publishing, Cham, pp. 133–161. https://doi.org/10.1007/978-3-319-67774-3_6.

Ramos, V.A., 2010. The grenville-age basement of the andes. J. South Am. Earth Sci. 29, 77–91. https://doi.org/10.1016/j.jsames.2009.09.004.

Ramos, V.A., 2008. The basement of the central andes: the Arequipa and related terranes. Annu. Rev. Earth Planet Sci. 36, 289–324. https://doi.org/10.1146/annurev.earth.36.031207.124304.

Redwood, S.D., Rice, C.M., 1997. Petrogenesis of Miocene basic shoshonitic lavas in the Bolivian Andes and implications for hydrothermal gold, silver and tin deposits. J. South Am. Earth Sci. 10, 203–221. https://doi.org/10.1016/S0895-9811(97)00024-2.

Richards, J.P., Ullrich, T., Kerrich, R., 2006. The Late Miocene–Quaternary Antofalla volcanic complex, southern Puna, NW Argentina: protracted history, diverse petrology, and economic potential. J. Volcanol. Geoth. Res. 152, 197–239. https://doi.org/10.1016/j.jvolgeores.2005.10.006.

Richer, M., Mann, C.P., Stix, J., 2004. Mafic magma injection triggers eruption at Ilopango Caldera, El Salvador, Central America. In: Rose, W.I., Bommer, J.J., López, D.L., Carr, M.J., Major, J.J. (Eds.), Natural Hazards in El Salvador, Special Paper. Geological Society of America, Boulder, Colorado, pp. 175–189. https://doi.org/10.1130/0-8137-2375-2.175.

Riller, U., Petrinovic, I., Ramelow, J., Strecker, M., Oncken, O., 2001. Late Cenozoic tectonism, collapse caldera and plateau formation in the central Andes. Earth Planet Sci. Lett. 188, 299–311. https://doi.org/10.1016/S0012-821X(01)00333-8.

Risse, A., Trumbull, R.B., Coira, B., Kay, S.M., Bogaard, P. van den, 2008. 40Ar/39Ar geochronology of mafic volcanism in the back-arc region of the southern Puna plateau, Argentina. J. South Am. Earth Sci. 26, 1–15. https://doi.org/10.1016/j.jsames.2008.03.002.

Risse, A., Trumbull, R.B., Kay, S.M., Coira, B., Romer, R.L., 2013. Multi-stage evolution of late neogene mantle-derived magmas from the central andes back-arc in the southern Puna plateau of Argentina. J. Petrol. 54, 1963–1995. https://doi.org/10.1093/petrology/egt038.

Rodriguez-Gonzalez, A., Fernandez-Turiel, J.L., Perez-Torrado, F.J., Aulinas, M., Carracedo, J.C., Gimeno, D., Guillou, H., Paris, R., 2011. GIS methods applied to the degradation of monogenetic volcanic fields: a case study of the Holocene volcanism of Gran Canaria (Canary Islands, Spain). Geomorphology 134, 249–259. https://doi.org/10.1016/j.geomorph.2011.06.033.

Rodriguez-Gonzalez, A., Fernandez-Turiel, J.L., Perez-Torrado, F.J., Gimeno, D., Aulinas, M., 2010. Geomorphological reconstruction and morphometric modelling applied to past volcanism. Int. J. Earth Sci. 99, 645–660. https://doi.org/10.1007/s00531-008-0413-1.

Rodriguez-Gonzalez, A., Fernandez-Turiel, J.L., Perez-Torrado, F.J., Paris, R., Gimeno, D., Carracedo, J.C., Aulinas, M., 2012. Factors controlling the morphology of monogenetic basaltic volcanoes: the Holocene volcanism of Gran Canaria (Canary Islands, Spain). Geomorphology 136, 31–44. https://doi.org/10.1016/j.geomorph.2011.08.023.

Roeder, P.L., Emslie, R.F., 1970. Olivine-liquid equilibrium. Contrib. Mineral. Petrol. 29, 275–289. https://doi.org/10.1007/BF00371276.
Salisbury, M.J., Kent, A.J.R., Jiménez, N., Jicha, B.R., 2015. Geochemistry and 40Ar/39Ar geochronology of lavas from Tunupa volcano, Bolivia: implications for plateau volcanism in the central Andean Plateau. Lithosphere 7, 95–107. https://doi.org/10.1130/L399.1.
Sandeman, H.A., Clark, A.H., 2004. Commingling and mixing of S-type peraluminous, ultrapotassic and basaltic magmas in the Cayconi volcanic field, Cordillera de Carabaya, SE Peru. Lithos 73, 187–213. https://doi.org/10.1016/j.lithos.2003.12.005.
Sato, H., 1975. Diffusion coronas around quartz xenocrysts in andesite and basalt from Tertiary volcanic region in northeastern Shikoku, Japan. Contrib. Mineral. Petrol. 50, 49–64.
Schnurr, W.B.W., Trumbull, R.B., Clavero, J., Hahne, K., Siebel, W., Gardeweg, M., 2007. Twenty-five million years of silicic volcanism in the southern central volcanic zone of the Andes: geochemistry and magma genesis of ignimbrites from 25 to 27 °S, 67 to 72 °W. J. Volcanol. Geoth. Res. 166, 17–46. https://doi.org/10.1016/j.jvolgeores.2007.06.005.
Schoenbohm, L.M., Carrapa, B., 2015. Miocene–Pliocene shortening, extension, and mafic magmatism support small-scale lithospheric foundering in the central Andes, NW Argentina. In: DeCelles, P.G., Ducea, M.N., Carrapa, B., Kapp, P.A. (Eds.), Geodynamics of a Cordilleran Orogenic System: the Central Andes of Argentina and Northern Chile, Memoir. Geological Society of America, pp. 168–181. https://doi.org/10.1130/2015.1212(09.
Schreiber, U., Schwab, K., 1991. Geochemistry of quaternary shoshonitic lavas related to the Calama-Olacapato-El Toro Lineament, NW Argentina. J. South Am. Earth Sci. 4, 73–85. https://doi.org/10.1016/0895-9811(91)90019-H.
Schurr, B., Rietbrock, A., Asch, G., Kind, R., Oncken, O., 2006. Evidence for lithospheric detachment in the central Andes from local earthquake tomography. Tectonophysics 415, 203–223. https://doi.org/10.1016/j.tecto.2005.12.007.
Schwab, K., Lippolt, H., 1974. K-Ar mineral ages and late Cenozoic history of the Salar de Cauchari area (Argentine Puna). In: Gonzalez-Ferran, O. (Ed.), Proceedings. Presented at the IAVCEI, Symposium on Andean and Antarctic Volcanology Problems, Santiago, Chile, pp. 698–714.
Seggiaro, R.E., Guzman, S., Pereyra, R., Coppolecchia, M., Cegarra, M., 2016. Neotectónica y volcanismo monogenético cuaternario sobre el segmento central del lineamiento Calama Olacapato Toro (COT). Rev. Asoc. Geol. Argent. 73, 468–477.
Sobolev, S.V., Babeyko, A.Y., 2005. What drives orogeny in the Andes? Geology 33, 617–620. https://doi.org/10.1130/G21557AR.1.
Sparks, R.S.J., Folkes, C.B., Humphreys, M.C.S., Barfod, D.N., Clavero, J., Sunagua, M.C., McNutt, S.R., Pritchard, M.E., 2008. Uturuncu volcano, Bolivia: volcanic unrest due to mid-crustal magma intrusion. Am. J. Sci. 308, 727. https://doi.org/10.2475/06.2008.01.
Steiger, R.H., Jäger, E., 1977. Subcommission on geochronology: convention on the use of decay constants in geo- and cosmochronology. Earth Planet Sci. Lett. 36, 359–362. https://doi.org/10.1016/0012-821X(77)90060-7.
Stern, C.R., 2004. Active Andean volcanism: its geologic and tectonic setting. Rev. Geol. Chile 31, 161–206. https://doi.org/10.4067/S0716-02082004000200001.
Stern, C.R., Moreno, H., López-Escobar coordinators, L., Clavero, J.E., Lara, L.E., Naranjo, J.A., Parada, M.A., Alexandra Skewes, M., 2007. Chilean volcanoes. In: Moreno, T., Gibbons, W. (Eds.), The Geology of Chile. Geological Society of London, pp. 147–178. https://doi.org/10.1144/GOCH.5.
Stewart, M.L., Pearce, T.H., 2004. Sieve-textured plagioclase in dacitic magma: interference imaging results. Am. Mineral. 89, 348–351. https://doi.org/10.2138/am-2004-2-313.
Straub, S., Gómez-Tuena, A., Stuart, F., Zellmer, G.F., Espinasa-Pereña, R., Cai, Y., Iizuka, Y., 2011. Formation of hybrid arc andesites beneath thick continental crust. Earth Planet Sci. Lett. 303, 337–347.
Streck, M., 2008. Mineral textures and zoning as evidence for open system processes. Rev. Mineral. Geochem. 69, 595–622.
Strecker, M.R., Alonso, R.N., Bookhagen, B., Carrapa, B., Hilley, G.E., Sobel, E.R., Trauth, M.H., 2007. Tectonics and climate of the southern central andes. Annu. Rev. Earth Planet Sci. 35, 747–787. https://doi.org/10.1146/annurev.earth.35.031306.140158.
Sun, C., Liang, Y., 2013. The importance of crystal chemistry on REE partitioning between mantle minerals (garnet, clinopyroxene, orthopyroxene, and olivine) and basaltic melts. Chem. Geol. 358, 23–36. https://doi.org/10.1016/j.chemgeo.2013.08.045.
Tannhäuser, F., 1906. Petrographische Untersuchungen an jungvulkanischen Gesteinen aus der argentinische Republik. Neues Jahrb. Min. Geol. Pal., Beil. - Bd. XXII, 555–638.
Thompson, R.N., Gibson, S.A., 2000. Transient high temperatures in mantle plume heads inferred from magnesian olivines in Phanerozoic picrites. Nature 407, 502–506. https://doi.org/10.1038/35035058.
Thorpe, R.S., 1984. The tectonic setting of active Andean volcanism. In: Harmon, R.S., Barreiro, B.A. (Eds.), Andean Magmatism: Chemical and Isotopic Constraints. Birkhäuser Boston, Boston, MA, pp. 4–8. https://doi.org/10.1007/978-1-4684-7335-3_1.
Tibaldi, A., Bonali, F.L., 2018. Contemporary recent extension and compression in the central Andes. J. Struct. Geol. 107, 73–92. https://doi.org/10.1016/j.jsg.2017.12.004.
Tibaldi, A., Bonali, F.L., Corazzato, C., 2017. Structural control on volcanoes and magma paths from local- to orogen-scale: the central Andes case. Tectonophysics 699, 16–41. https://doi.org/10.1016/j.tecto.2017.01.005.
Tilling, R.I., 2009. Volcanism and associated hazards: the Andean perspective. Adv. Geosci. 22, 125–137. https://doi.org/10.5194/adgeo-22-125-2009.
Tsuchiyama, A., 1985. Dissolution kinetics of plagioclase in the melt of the system diopside-albite-anorthite, and origin of dusty plagioclase in andesites. Contrib. Mineral. Petrol. 89, 1–16. https://doi.org/10.1007/BF01177585.
Urquizo Furlán, P.E., 2012. Mecanismos de erupción y modelo de facies del volcán monogenético Negro de Chorrillos, Puna salteña (Tesis de Grado). Universidad Nacional de Salta, Salta, Argentina.
Viccaro, M., Giacomoni, P.P., Ferlito, C., Cristofolini, R., 2010. Dynamics of magma supply at Mt. Etna volcano (Southern Italy) as revealed by textural and compositional features of plagioclase phenocrysts. Lithos 116, 77–91. https://doi.org/10.1016/j.lithos.2009.12.012.
Vilela, C.R., 1969. Descripcion geologica de la hoja 6c, San Antonio de los Cobres. Provincias de Salta y Jujuy. Escala 1:200.000. Carta Geológico-Económica de la República Argentina.
Wei, F., Prytulak, J., Xu, J., Wei, W., Hammond, J.O.S., Zhao, B., 2017. The cause and source of melting for the most recent volcanism in Tibet: a combined geochemical and geophysical perspective. Lithos 288–289, 175–190. https://doi.org/10.1016/j.lithos.2017.07.003.
Winter, J.D., 2010. Principles of Igneous and Metamorphic Petrology, second ed. Pearson.
The puu oo eruption of kilauea volcano, Hawaii; episodes 1 through 20, January 3, 1983, through June 8, 1984. In: Wolfe, E.W. (Ed.), U. S. Geol. Surv. Prof. Pap. 1463, 1–251. https://doi.org/10.3133/pp1463.
Wörner, G., 2019. The roots of volcanism in the Central Andes. Geophys. Res. Abstr. 21, EGU2019–18587.
Wörner, G., Mamani, M., Blum-Oeste, M., 2018. Magmatism in the central andes. Elements 14, 237–244. https://doi.org/10.2138/gselements.14.4.237.
Yuan, X., Sobolev, S.V., Kind, R., 2002. Moho topography in the central Andes and its geodynamic implications. Earth Planet Sci. Lett. 199, 389–402. https://doi.org/10.1016/S0012-821X(02)00589-7.
Zhang, B., Hu, X., Li, P., Tang, Q., Zhou, W., 2019. Trace element partitioning between amphibole and hydrous silicate glasses at 0.6–2.6 GPa. Acta Geochimica 38, 414–429. https://doi.org/10.1007/s11631-019-00322-4.